Precision Engineering 66 (2020) 429–444

Contents lists available at ScienceDirect

Precision Engineering

journal homepage: www.elsevier.com/locate/precision

A spatial closed-form nonlinear stiffness model for sheet flexures based on a mixed variational principle including third-order effects

M. Nijenhuis *, J.P. Meijaard, D.M. Brouwer

Precision Engineering, Faculty of Engineering Technology, University of Twente, Drienerlolaan 5, 7522 NB Enschede, The Netherlands

ARTICLE INFO

Keywords:
Flexure mechanism
Analytical model
Geometric stiffness
Nonlinear analysis
Closed-form
Sheet flexure
Flexure strip
Leaf spring

ABSTRACT

The sheet flexure is commonly used to provide support stiffness in flexure mechanisms for precision applications. While the sheet flexure is often analyzed in a simplified form, e.g. by assuming planar deformation or linearized stiffness, the deformation in practice is spatial and sufficiently large that nonlinear effects due to the geometric stiffness are significant.

This paper presents a compact analytical model for the nonlinear stiffness characteristics of spatially deforming sheet flexures under general 3-D load conditions at moderate deformations. This model provides closed-form expressions in a mixed stiffness and compliance matrix format that is tailored to flexure mechanism analysis. The effects of bending, shear, elongation, torsion and warping deformation are taken into account, so that the stiffness in all directions, including the in-plane lateral support direction, is modeled accurately. The model is verified numerically against beam and shell-based finite elements. The approach for deriving closed-form solutions in a nonlinear context is detailed in this paper. The Hellinger–Reissner variational principle with a specific physically motivated set of low-order interpolation functions is shown to be well-suited to the geometrically nonlinear analysis of flexures.

An extension of the derivation approach to the nonlinear closed-form analysis of general flexure mechanisms consisting of multiple sheet flexures connected in parallel is presented. This is demonstrated with the case of a spatially deforming parallelogram flexure mechanism and a cross-hinge flexure mechanism.

1. Introduction

Flexure mechanisms are used in precision applications for their predictable behavior [1–4]. Like traditional rigid-link mechanisms, they are essentially motion guiding mechanisms: they allow motion in some directions, while providing load-carrying support in others. Unlike traditional linkages though, flexure mechanisms rely on the elastic deformation of components. This means that their operation is almost hysteresis-free, backlash-free, limited in range, and governed only by stiffness properties.

A typical flexure mechanism has a stage, whose motion is dictated by various elastic components that are attached to it in parallel and series configurations. In some directions, the components provide relatively high stiffness in order to constrain the stage motion (and provide load-carrying support), while in the directions of desired stage motion, the components add only low stiffness. From a designer's point of view, the elastic components are considered to be constraint elements.

A common elastic component is the *sheet flexure* (also referred to as a leaf spring, flexure strip or flexure blade), depicted in Fig. 1, that serves as a constraint element between rigid bodies A and B. Its thickness is typically one or more orders of magnitude smaller than its length and width. As a consequence of that shape, the sheet flexure constrains the relative motion (i.e. provides high stiffness) in the translational x-, z- and rotational y-directions, while allowing the relative motion (i.e. adding only low stiffness) in the rotational x-, z- and translational y-directions. The directions of constraint are also referred to as *support directions*; the directions of intended motion as *degrees of freedom* (DOFs).

Inherent to the sheet flexure is that the desired high stiffness in the support directions decreases when it deflects in a DOF [5], which is referred to as an *elastokinematic* effect [6]. This poses a direct limitation on the performance. A related but less critical observation is that the desired low stiffness in the DOFs changes with the applied loads. These nonideal constraint characteristics of the sheet flexure stem from the configuration-dependent geometric stiffness. They are relevant to the design of flexure mechanisms with a large range of motion, and constitute the topic of this work.

The predictable nature of sheet flexures means that the governing equations of solid mechanics deliver accurate results, e.g. when used

* Corresponding author.
E-mail address: m.nijenhuis@utwente.nl (M. Nijenhuis).

https://doi.org/10.1016/j.precisioneng.2020.08.003
Received 7 March 2020; Received in revised form 3 July 2020; Accepted 5 August 2020
Available online 10 August 2020

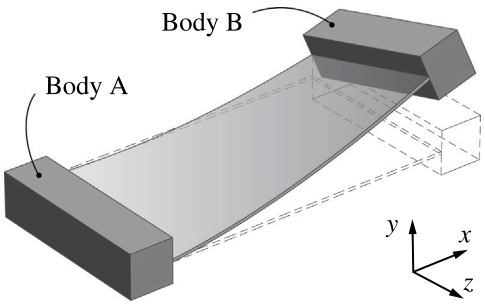

Fig. 1. A sheet flexure constraining motion between rigid bodies A and B.

in a discretized form in the ubiquitous finite element method. To actually inform design decisions, we seek to develop a parametric model instead. A mathematical model that is accurate and understandable conveys how design parameters affect the nonideal constraint characteristics in ways that the 3-D elasticity differential equations or the finite element analysis of a particular design cannot.

For an overview of the solid mechanics theories that govern structures similar to the sheet flexure, the reader is referred to Sen [7]. In the literature on flexure mechanisms, parametric models for some typical elastic components can be found. The beam constraint model for planar (2-D) sheet flexures considers loads and deformation limited to the x, y-plane of Fig. 1 [8,9]. It captures the relevant nonlinearities due to the geometrical stiffness in a closed-form format. A similar model for wire flexures with isotropic cross-section (e.g. a round or square cross-section) that does consider general spatial (3-D) loads and deformation has been developed [10]. An extension to rectangular cross-sections is also available [11], but limited to small width-to-length ratios, since shear and constrained warping have not been accounted for. Consequently, it does not accurately model the lateral constraint directions of the sheet flexure, which as a constraint element is designed to provide high stiffness in those directions by means of a large width-to-length ratio.

Parametric models for the spatial sheet flexure are only available for a specific loading condition (a lateral load) and a limited twist angle [12,13]. For the parallelogram flexure mechanism specifically, parametric expressions of the geometrically nonlinear stiffness are available [14]. A method for obtaining the spatial deformation of a sheet flexure in an iterative–analytical fashion has been proposed, but not applied to the development of a general closed-form parametric model [15].

The contribution of this work is a closed-form parametric model for the general spatial deformation encountered in sheet flexures. In this paper, we present:

1. an energy-based approach for the formulation of a closed-form model using the Hellinger–Reissner variational principle,
2. the treatment of bending, torsion, elongation, shear and warping deformation, including third-order geometrically nonlinear effects,
3. understandable closed-form expressions that model the nonideal constraint characteristics of sheet flexures in terms of support stiffness, loads in the DOFs, and potential energy,
4. a verification by means of a commercial finite element code,
5. an energy-based procedure for the closed-form analysis of general assemblies of sheet flexures connected in parallel, and
6. the application to the case of a spatially deforming parallelogram flexure mechanism and cross-hinge mechanism.

2. Method

The development of solid mechanics models involves a trade-off between accuracy and complexity of the resulting formulation. Since we aim to develop a model that can inform design decisions, it should be minimally complex, i.e. be represented by mathematically simple closed-form expressions. To that end, we adopt the reduced model of beam theory (with only a single independent coordinate) rather than that of plate theory (with still two independent coordinates) or full 3-D elasticity theory (with three independent coordinates) [16,17]. Previous work on flexure mechanism models has also indicated that beam theory is sufficiently accurate for shapes and loads of practical interest at only limited complexity [7,14,15]. Furthermore, the current work focuses solely on the static behavior of sheet flexures, so inertia effects are disregarded.

The following Section 2.1 is an overview of the equations that govern general spatial (3-D) geometrically nonlinear deformation of a beam. These are commonly used and summarized here only to establish the notation, sign and symbol convention that is used in the development of the sheet flexure formulation in the sections after that.

2.1. Beam kinematics

2.1.1. Deformed configuration

The configuration of a deformed beam can be represented by its elastic line and the cross-sectional planes attached to it (see Fig. 2) [18]. The independent coordinate $s \in [0, L]$ measures the distance along the undeformed elastic line. The orientation of the cross-section at an arbitrary point on the elastic line is described by a set of three orthonormal vectors, as shown in Fig. 2c: $\mathbf{e}_{\bar{x}}$ is normal to the cross-sectional plane, $\mathbf{e}_{\bar{y}}$ and $\mathbf{e}_{\bar{z}}$ are along the principal axes of the cross-sectional plane.

A fixed coordinate frame is attached to the beam at $s = 0$ in the same manner and denoted by base vectors $\mathbf{e}_x$, $\mathbf{e}_y$ and $\mathbf{e}_z$ (without overbar). All vectors in the current analysis are resolved in this frame unless noted otherwise. The local ('moving') frame $\mathbf{e}_{\bar{x}}, \mathbf{e}_{\bar{y}}, \mathbf{e}_{\bar{z}}$ is related to the fixed frame $\mathbf{e}_x, \mathbf{e}_y, \mathbf{e}_z$ by a rotation matrix, dependent on s, according to

$$\underbrace{\begin{bmatrix}\mathbf{e}_{\bar{x}} & \mathbf{e}_{\bar{y}} & \mathbf{e}_{\bar{z}}\end{bmatrix}}_{\substack{\text{local frame attached}\\ \text{to deformed cross-section}}} = \mathbf{R}(s) \underbrace{\begin{bmatrix}\mathbf{e}_x & \mathbf{e}_y & \mathbf{e}_z\end{bmatrix}}_{\text{fixed frame}}. \tag{1}$$

The position of the elastic line, shown in Fig. 2b, with respect to the fixed frame is given by

$$\mathbf{r}(s) = \mathbf{r}_0(s) + \mathbf{u}(s) = s\,\mathbf{e}_x + \begin{bmatrix}\mathbf{e}_x & \mathbf{e}_y & \mathbf{e}_z\end{bmatrix}\begin{bmatrix}u_x(s)\\ u_y(s)\\ u_z(s)\end{bmatrix}, \tag{2}$$

where $\mathbf{u}(s)$ is the displacement vector.

As a parametrization for the cross-sectional orientation matrix $\mathbf{R}(s)$, we choose the three Tait–Bryan (Euler) angles $\phi_x(s)$, $\phi_y(s)$ and $\phi_z(s)$ in the specific order

$$\mathbf{R}(s) = \begin{bmatrix}\cos\phi_y & 0 & \sin\phi_y\\ 0 & 1 & 0\\ -\sin\phi_y & 0 & \cos\phi_y\end{bmatrix}\begin{bmatrix}\cos\phi_z & -\sin\phi_z & 0\\ \sin\phi_z & \cos\phi_z & 0\\ 0 & 0 & 1\end{bmatrix}\begin{bmatrix}1 & 0 & 0\\ 0 & \cos\phi_x & -\sin\phi_x\\ 0 & \sin\phi_x & \cos\phi_x\end{bmatrix}. \tag{3}$$

The angles describe the rotation with respect to and resolved in the fixed frame denoted by $\mathbf{e}_x$, $\mathbf{e}_y$ and $\mathbf{e}_z$. The choice of the rotation order does not affect the accuracy of the model; it does affect the difficulty of the mathematical steps involved at a later stage, as will be detailed in Section 2.6.

The configuration of a deformed beam is thus given by the elastic line position, described by the displacements $u_x(s)$, $u_y(s)$, $u_z(s)$, and the cross-sectional orientation, described by the angles $\phi_x(s)$, $\phi_y(s)$ and $\phi_z(s)$.

2.1.2. Deformation measures

In terms of the six functions that describe the beam configuration (see Section 2.1.1), six independent measures of deformation can be

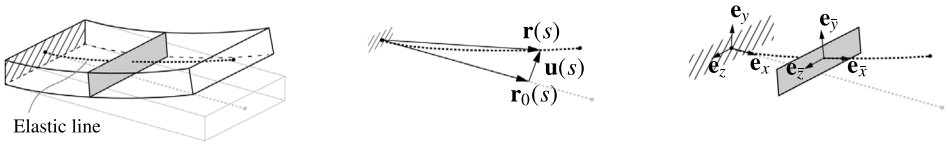

(a) Sheet flexure modeled as a beam (thickness exaggerated).

(b) Position of the elastic line.

(c) Orientation of a cross-section.

Fig. 2. Kinematic description of a deformed sheet flexure, modeled as a beam. Image reused from the authors' previous work [12,13].

identified for a beam that is capable of bending, extension, torsion and shear deformation [19].

The skew-symmetric matrix

$$\boldsymbol{\kappa}(s) = \mathbf{R}^T\mathbf{R}' = \begin{bmatrix} 0 & -\kappa_{\bar{z}} & \kappa_{\bar{y}} \\ \kappa_{\bar{z}} & 0 & -\kappa_{\bar{x}} \\ -\kappa_{\bar{y}} & \kappa_{\bar{x}} & 0 \end{bmatrix} \tag{4}$$

contains the three independent curvatures, given by the expressions

$$\begin{aligned} \kappa_{\bar{x}}(s) &= \phi_x' + \phi_y' \sin\phi_z \approx \phi_x' + \phi_y'\phi_z, \\ \kappa_{\bar{y}}(s) &= \phi_y' \cos\phi_x \cos\phi_z + \phi_z' \sin\phi_x \approx \phi_y' + \phi_z'\phi_x, \\ \kappa_{\bar{z}}(s) &= \phi_z' \cos\phi_x - \phi_y' \sin\phi_x \cos\phi_z \approx \phi_z' - \phi_y'\phi_x, \end{aligned} \tag{5}$$

truncated after the second-order term. A prime denotes a derivative with respect to the distance s along the undeformed elastic line. As measures of deformation, $\kappa_{\bar{x}}$ represents the specific twist angle of the beam, $\kappa_{\bar{y}}$ the curvature in the $\mathbf{e}_{\bar{x}}, \mathbf{e}_{\bar{z}}$-plane, and $\kappa_{\bar{z}}$ the curvature in the $\mathbf{e}_{\bar{x}}, \mathbf{e}_{\bar{y}}$-plane.

The strains are given by the vector

$$\boldsymbol{\gamma}(s) = \mathbf{R}^T\left(\mathbf{e}_x + \mathbf{u}' - \mathbf{e}_{\bar{x}}\right), \tag{6}$$

which consists of the three components

$$\begin{aligned} \gamma_{\bar{x}}(s) &\approx u_x' - \phi_y\left(\phi_y/2 + u_z'\right) - \phi_z\left(\phi_z/2 - u_y'\right), \\ \gamma_{\bar{y}}(s) &\approx u_y' - \phi_z\left(1 + u_x'\right) + \phi_x\left(\phi_y + u_z'\right), \\ \gamma_{\bar{z}}(s) &\approx u_z' + \phi_y\left(1 + u_x'\right) + \phi_x\left(\phi_z - u_y'\right), \end{aligned} \tag{7}$$

truncated after the second-order terms. Here, $\gamma_{\bar{x}}$ represents the axial strain of the elastic line, $\gamma_{\bar{y}}$ the shear angle in the $\mathbf{e}_{\bar{x}}, \mathbf{e}_{\bar{y}}$-plane, and $\gamma_{\bar{z}}$ the shear angle in the $\mathbf{e}_{\bar{x}}, \mathbf{e}_{\bar{z}}$-plane.

In their non-linearized form, the finite strain and curvature measures of Eqs. (5) and (7) are referred to as the compatibility equations and account for geometrically nonlinear effects.

An effect that is not captured by $\boldsymbol{\gamma}$ is the coupling between elongation and torsion, sometimes referred to as the trapeze effect or Wagner effect. It describes the shortening of a beam being twisted and the torsional buckling due to an axial load [20,21]. We account for this effect by modifying and augmenting the axial strain $\gamma_{\bar{x}}$ with the term $I_{\text{te}}\phi_x'^2/2$, where

$$I_{\text{te}} = \left(w^2 + t^2\right)/12 \tag{8}$$

for a rectangular cross-section with width w and thickness t. This effect was also considered by Sen and Awtar in the model for wire flexures with isotropic cross-sections [10].

2.1.3. Constitutive relations

Linear material behavior for rectangular cross-sections is governed by

$$\begin{aligned} F_{\bar{x}}(s) &= EA\gamma_{\bar{x}}(s), & M_{\bar{y}}(s) &= EI_y\kappa_{\bar{y}}(s), \\ F_{\bar{y}}(s) &= kGA\gamma_{\bar{y}}(s), & M_{\bar{z}}(s) &= EI_z\kappa_{\bar{z}}(s), \\ F_{\bar{z}}(s) &= kGA\gamma_{\bar{z}}(s), & B(s) &= EI_w\kappa_{\bar{x}}'(s), \end{aligned} \tag{9}$$

and the linear ordinary differential equation

$$M_{\bar{x}}(s) = GJ\kappa_{\bar{x}}(s) - EI_w\kappa_{\bar{x}}''(s), \tag{10}$$

where $F_{\bar{x}}$ is the axial force, $F_{\bar{y}}$ and $F_{\bar{z}}$ are the transverse forces, $M_{\bar{x}}$ is the torsion moment, $M_{\bar{y}}$ and $M_{\bar{z}}$ are the bending moments, and B is the bimoment. The parameters are Young's modulus E, the cross-sectional area A, the second moments of area about the principal axes I_y and I_z, the shear correction factor k [22], the shear modulus G, Saint-Venant's torsion constant J, and Vlasov's warping constant I_w, which is given by [23]

$$I_w = w^3t^3/144. \tag{11}$$

2.2. Static equilibrium principles

The static equilibrium configuration that a beam assumes when subjected to applied forces and moments (collectively referred to as loads) is described by various equilibrium principles. One approach for finding the equilibrium configuration is to formulate force and moment balance equations of an infinitesimal-length beam segment; combined with compatibility and constitutive relations, they lead to a coupled system of nonlinear (ordinary) differential equations. Only upon (partial) linearization can exact solutions to these ODEs be obtained. Another approach is to consider the entire beam domain, instead of an infinitesimal segment, and use interpolation functions to obtain a system of algebraic equations that is potentially solvable. Energy methods, such as the principle of minimum total potential energy (essentially a virtual work principle for conservative systems), can be useful for the purpose of interpolation or discretization [24].

When linear theory suffices and the errors associated with a fully linearized beam model are acceptable, the two approaches can be used without mathematical difficulty. However, when geometrically nonlinear effects are relevant, such as in the present work in which stiffness changes with deflection, the governing differential equations can pose difficulties.

Both approaches can be found in the literature on flexure mechanism analysis. In the development of a planar (2-D) model for sheet flexures, Awtar et al. consider a system of partly linearized ODEs that admits an exact solution for the displacement fields, which happens to be transcendental in one of the applied loads [8]. A useful closed-form model has nevertheless been obtained since the exact solution is well approximated by a truncated series expansion. In turn, with that solution, a strain energy expression has been formulated, which is convenient for reducing the mathematical complexity when dealing with multi-flexure mechanisms (as per the principle of virtual work in which constraint forces do no work) [25]. Along the same lines, Sen and Awtar have developed a spatial (3-D) model for slender beam-like flexures restricted to isotropic cross-sections ($I_y = I_z$) [10]. Bai et al. have produced an extension to rectangular cross-sections by means of a power series solution to the ODEs; it is restricted to small w/L because it does not account for shear and warping deformation [11].

Typical sheet flexures, though, are one or more orders of magnitude wider than they are thick, in order to provide adequate lateral support stiffness. In pursuit of a spatial model for sheet flexures, Sen has formulated a simplified governing system of ODEs, but with still too much complexity (variable coefficients) for an exact solution [7]. Van Eijk has described the governing equations as a system of nonlinear integro-differential equations and demonstrated an iterative–analytical method for approximating the solution based on initial estimates of

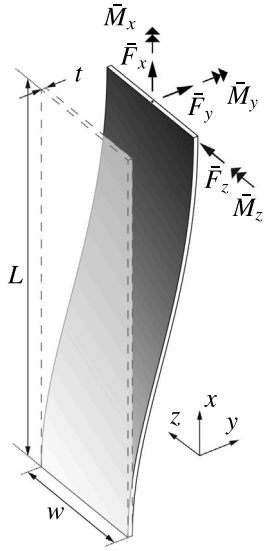

Fig. 3. Fixed-free sheet flexure subject to an arbitrary spatial end-load.

interpolation functions [15]. Although the method has been validated for several specific load cases of the sheet flexure and some common flexure mechanisms, it has not been applied to the development of a sheet flexure model for a general load case. Nijenhuis et al. have formulated spatial models for specific cases. A closed-form expression has been obtained for a lateral loading condition by means of a finite element-like discretization and simultaneous interpolation of the moment and displacement fields [12]. The model has been extended for a general loading condition but with a limited twist angle [13]. Based on observations in these last publications, we now follow a different approach and construct the desired closed-form spatial sheet flexure model.

When the principle of virtual work is applied to the system's total potential energy functional, the ODEs that are obtained in the variation process (the Euler–Lagrange equations) make the functional stationary and represent the strong form of the equilibrium conditions for the beam. While the ODE is exact, in the sense that it represents the equilibrating solution for each point in the domain, exactness is not a requirement for a useful model in the context of flexure mechanism analysis; given the observed difficulties associated with solutions to such ODEs (and the relative value of an 'exact' solution in an approximate theory such as beam theory), we instead use the system's total potential energy functional with a variational principle to approximate the solution by means of suitably chosen interpolation functions (also referred to as test or trial functions). The accuracy and complexity of the resulting sheet flexure formulation are then determined by the choice of interpolation functions and the type of variational principle. An important advantage of the energy-based approximation is the availability of the potential energy scalar, from which the model equations are derived: it can be used to compare the magnitude of effects and provide the justification for the consistent truncation of terms. This is an advantage over earlier interpolation-based methods that did not use a potential energy scalar [12,13,15].

In the typical principle of minimum total potential energy, the variations of the functional are carried out with respect to the displacement field. The (kinematically admissible) displacement field that makes the potential energy stationary is the physical one. In previous work, it has been observed that the displacement fields of flexure elements become explicitly dependent on applied load parameters when a nonlinear contribution of the geometric stiffness is accounted for. It then makes sense to use a variational principle that not only considers variations of the displacement field, but simultaneous variations of the internal moment field as well. The Hellinger–Reissner variational principle is such a principle [26].

2.3. Hellinger–Reissner variational principle

The potential energy associated with the Hellinger–Reissner variational principle for a sheet flexure, see Fig. 3, is expressed as

$$P = P_{\text{int}} - W_{\text{ext}}, \tag{12}$$

where the internal energy is

$$\begin{aligned} P_{\text{int}} = B(L)\kappa_{\bar{x}}(L) + \int_0^L \Bigg[& M_{\bar{x}}\kappa_{\bar{x}} - \frac{\left(M_{\bar{x}} + B'\right)^2}{2GJ} - \frac{B^2}{2EI_w} && \text{nonuniform torsion} \\ & + M_{\bar{y}}\kappa_{\bar{y}} - \frac{M_{\bar{y}}^2}{2EI_y} && \text{bending } \mathbf{e}_{\bar{x}}, \mathbf{e}_{\bar{z}} \text{ plane} \\ & + M_{\bar{z}}\kappa_{\bar{z}} - \frac{M_{\bar{z}}^2}{2EI_z} && \text{bending } \mathbf{e}_{\bar{x}}, \mathbf{e}_{\bar{y}} \text{ plane} \\ & + F_{\bar{x}}\gamma_{\bar{x}} - \frac{F_{\bar{x}}^2}{2EA} && \text{elongation} \\ & + F_{\bar{y}}\gamma_{\bar{y}} - \frac{F_{\bar{y}}^2}{2kGA} && \text{shear } \mathbf{e}_{\bar{x}}, \mathbf{e}_{\bar{y}} \text{ plane} \\ & + F_{\bar{z}}\gamma_{\bar{z}} - \frac{F_{\bar{z}}^2}{2kGA} \Bigg] \mathrm{d}s. && \text{shear } \mathbf{e}_{\bar{x}}, \mathbf{e}_{\bar{z}} \text{ plane} \end{aligned} \tag{13}$$

The potential energy P is a functional of both the displacement (and rotation) fields and moment (and force) fields. The curvatures $\kappa_{\bar{x}}, \kappa_{\bar{y}}, \kappa_{\bar{z}}$ and strains $\gamma_{\bar{x}}, \gamma_{\bar{y}}, \gamma_{\bar{z}}$ in P_{int} are related to the displacements and rotations by Eqs. (5) and (7). This formulation is based on Timoshenko beam theory with nonuniform torsion.

The Hellinger–Reissner principle states that P is rendered stationary by those displacement and moment fields that are the physical ones [26]. In other words, the beam is in equilibrium when the variation of P with respect to the independent displacement and moment fields vanishes. Compared with the principle of minimum total potential energy, in which the displacements are the only independent fields and variations yield the equilibrium equations, the Hellinger–Reissner principle also encodes the compatibility equations as variations with respect to the moment fields.

A physical interpretation of the terms of P_{int} is given alongside the expression. It shows that the internal energy due to the various deformation modes of bending, shear, torsion and elongation can simply be added. The derivation of the terms that account for nonuniform torsion, involving the torsion moment $M_{\bar{x}}$ and bimoment B, is detailed in Appendix A.1.

By interpolating the internal moment and displacement fields using suitable interpolation functions with unknown coefficients, the integral in P can be evaluated. The variations with respect to the unknown displacement coefficients then yield a system of algebraic equilibrium equations; the variations with respect to the unknown moment coefficients yield a system of algebraic compatibility equations. Both systems are expressed in terms of the unknown interpolation coefficients and can potentially be solved for the parameters of interest. This approach will be detailed in the following sections.

The external work in P of Eq. (12) is

$$\begin{aligned} W_{\text{ext}} = {} & \bar{M}_x^{\text{TB}}\phi_x(L) + \bar{M}_y^{\text{TB}}\phi_y(L) + \bar{M}_z^{\text{TB}}\phi_z(L) \\ & + \bar{F}_x u_x(L) + \bar{F}_y u_y(L) + \bar{F}_z u_z(L) + \bar{B}\kappa_{\bar{x}}(L). \end{aligned} \tag{14}$$

Note that the internal loads $M_{\bar{x}}$, $M_{\bar{y}}$, $M_{\bar{z}}$, $F_{\bar{x}}$, $F_{\bar{y}}$, $F_{\bar{z}}$ and curvatures in the integrand are with respect to the *local frame* $\mathbf{e}_{\bar{x}}, \mathbf{e}_{\bar{y}}, \mathbf{e}_{\bar{z}}$ that is attached to the deformed cross-section (see Section 2.1.1). Since the displacements in the external work terms are chosen to be defined in the *fixed frame* $\mathbf{e}_x, \mathbf{e}_y, \mathbf{e}_z$, the associated (energetically-dual) applied

forces are also resolved in this fixed frame. Since the angles ϕ_x, ϕ_y and ϕ_z are Tait–Bryan angles, the associated moments $\bar{M}_x^{\mathrm{TB}}$, $\bar{M}_y^{\mathrm{TB}}$ and $\bar{M}_z^{\mathrm{TB}}$ are energetically dual to those angles, meaning that these moments are not the same as the components of the moment vector $[\bar{M}_x, \bar{M}_y, \bar{M}_z]$ resolved in the fixed frame. The first-order transformation is given by

$$\begin{aligned} \bar{M}_x^{\mathrm{TB}} &= \bar{M}_x + \bar{M}_y\phi_z(L) - \bar{M}_z\phi_y(L), \\ \bar{M}_y^{\mathrm{TB}} &= \bar{M}_y, \\ \bar{M}_z^{\mathrm{TB}} &= \bar{M}_z + \bar{M}_x\phi_y(L). \end{aligned} \tag{15}$$

This transformation cannot be applied directly to W_{ext} at the potential energy level, since $\bar{M}_x$, $\bar{M}_y$ and $\bar{M}_z$ are non-conservative loads; only after taking variations of P can the transformation be applied to the resulting strong form of the equations. In the remainder of this work, the moment vector components will be used, unless noted otherwise.

2.4. Order of magnitude estimates

To help choose the interpolation functions, estimates of the order of magnitude of the terms in the potential energy are useful. The complexity and accuracy of the formulation can then be controlled by retaining only those terms that are significant. We will proceed by stating a small number of assumptions, and apply criteria of maximum stress and buckling to estimate the magnitude of the various geometrical parameters, displacement vector components, deformation measures and loads. These estimates are expressed in terms of a small quantity so that truncation based on the relative powers of this quantity can be justified.

2.4.1. Assumptions

Regarding the geometry, deformation and material of the sheet flexure geometry, it is assumed that

- the width w is the same order as the length L;
- the transverse end-displacement $u_y(L)$ is limited to $0.15L$. The number

$$u = 0.15 \tag{16}$$

  is introduced as a small numerical quantity. All estimates in the following section are expressed in terms of powers of u in order to compare relative magnitudes;
- the failure strain ε of the material is at most 0.3%, which is considered a realistic failure strain for high tensile strength metals. In terms of powers of the small numerical constant u, the magnitude of ε is therefore estimated as u^3, which is approximately 0.003 (rather than e.g. u^2 or u^4). Note that this does not imply an algebraic relationship between ε and $u_y(L)$: estimating the magnitude of ε as u^3 here only implies that ε is closer to the numerical value of $u^3 \approx 0.003$ than to $u^2 \approx 0.02$ or $u^4 \approx 0.0005$.

In the following sections, the magnitude of the various geometrical parameters, loads and deformation measures is estimated in terms of powers of the numerical constant u, by applying the criteria of maximum stress and buckling.

2.4.2. Maximum stress criterion

Four different maximum stress cases are examined to estimate, first, the thickness t, the curvature $\kappa_{\bar{y}}$ and the specific twist angle $\kappa_{\bar{x}}$, and, second, the corresponding internal moments. The yield stress εE is considered to be the maximum allowed stress in the material.

1. Bending in the $\mathbf{e}_{\bar{x}}, \mathbf{e}_{\bar{y}}$-plane:
   An estimate for the magnitude of the thickness t can be obtained by considering the stress due to bending in the $\mathbf{e}_{\bar{x}}, \mathbf{e}_{\bar{y}}$-plane. It is assumed that the thickness of the sheet flexure is chosen such that the maximum allowed stress state occurs for a transverse displacement $u_y(L)$ of magnitude uL.
   Then, assuming a constant moment load $M_{\bar{z}} = 2EI_z u/L$, it follows that the bending stress $M_{\bar{z}}t/2I_z$ is equal to the yield stress εE when the thickness has magnitude $L\varepsilon/u = u^2 L$. Also, it then follows that the corresponding magnitude of $M_{\bar{z}}$ is EL^3u^7.
2. Bending in the $\mathbf{e}_{\bar{x}}, \mathbf{e}_{\bar{z}}$-plane:
   An estimate for the magnitude of the curvature $\kappa_{\bar{y}}$ can be obtained by considering the stress due to bending in the $\mathbf{e}_{\bar{x}}, \mathbf{e}_{\bar{z}}$-plane. It is assumed that the magnitude of the curvature $\kappa_{\bar{y}}$ is such that the maximum allowed stress state occurs for a corresponding bending moment of $M_{\bar{y}} = EI_y\kappa_{\bar{y}}$.
   It then follows that the bending stress $M_{\bar{y}}w/2I_y$ is equal to the yield stress εE when the curvature $\kappa_{\bar{y}}$ has magnitude $\varepsilon/L = u^3/L$. Also, it then follows that the corresponding magnitude of $M_{\bar{y}}$ is EL^3u^5.
3. Torsion:
   An estimate for the magnitude of the specific twist angle $\kappa_{\bar{x}}$ can be obtained by considering the stress due to torsion. It is assumed that the magnitude of the specific twist angle $\kappa_{\bar{x}}$ is such that the maximum allowed stress state occurs for a corresponding torsion moment of $M_{\bar{x}} = GJ\kappa_{\bar{x}}$.
   It then follows that the von Mises stress $\sqrt{3}|\tau_{\max}| = \sqrt{3}Gt|\kappa_{\bar{x}}|$ is equal to the yield stress $\varepsilon E \approx 3\varepsilon G$ when the specific twist angle $\kappa_{\bar{x}}$ has magnitude u/L. Also, it then follows that the corresponding magnitude of $M_{\bar{x}}$ is EL^3u^7.
4. Elongation:
   The magnitude of the axial strain $\gamma_{\bar{x}}$ is assumed to be ε at the maximum allowed stress state. The corresponding magnitude of internal axial load $F_{\bar{x}} = EA\gamma_{\bar{x}}$ is estimated as EL^2u^5.

2.4.3. Buckling criterion

When loads reach a critical value, elastic instability can occur [21]. With the stress criterion, this poses an additional limit on the magnitude of the loads and serves as a practical estimate. We estimate that the magnitude of the loads is at least one order smaller than the buckling load magnitude.

1. Euler column buckling:
   Buckling occurs when the axial load $\bar{F}_x$ reaches the critical value of $-c\pi^2 EI_z/L^2$ (where c depends on the boundary conditions), which has magnitude EL^2u^6. Force $\bar{F}_x$ is therefore estimated, one order smaller, as EL^2u^7.
2. Lateral buckling due to $\bar{F}_z$:
   Buckling occurs when the lateral load $\bar{F}_z$ reaches the critical value of $c\sqrt{EI_zGJ}/L^2$, which has magnitude EL^2u^6. Force $\bar{F}_z$ is therefore estimated as EL^2u^7.
3. Lateral buckling due to $\bar{M}_y$:
   Similar to lateral buckling due to $\bar{F}_z$, the magnitude of moment $\bar{M}_y$ is estimated as EL^3u^7.

2.4.4. Displacements and rotations

Given the maximum magnitude of the transverse displacement $u_y(L)$, the small-angle approximation $\phi_z \approx u_y'$ is valid (neglecting shear): the angle ϕ_z has magnitude u. The linear approximations $\kappa_{\bar{x}} \approx \phi_x'$, $\kappa_{\bar{y}} \approx \phi_y'$ and $\kappa_{\bar{z}} \approx \phi_z'$ can be combined with the second-order compatibility relations of Eq. (5) to find that

$$\kappa_{\bar{z}} \approx \phi_z' - \phi_y'\phi_x \approx \phi_z/L - \kappa_{\bar{y}}\kappa_{\bar{x}}L \sim u/L, \tag{17}$$

$$\phi_x' \approx \kappa_{\bar{x}} - \phi_y'\phi_z \approx \kappa_{\bar{x}} - \kappa_{\bar{y}}\kappa_{\bar{z}}L \sim u/L, \tag{18}$$

$$\phi_y' \approx \kappa_{\bar{y}} - \phi_z'\phi_x \approx \kappa_{\bar{y}} - \kappa_{\bar{z}}\kappa_{\bar{x}}L \sim u^2/L, \tag{19}$$

where differentiation and integration with respect to s are approximated by division and multiplication with L, respectively. In this fashion, the magnitude of the associated displacements and rotations can be estimated, as summarized in Table 1. Then, with the strain relation of Eq. (7), it follows that $u_x' \approx \gamma_{\bar{x}} - (u_y')^2/2 - (u_z')^2/2 \sim u^2$ and $u_x \sim u^2 L$.

2.4.5. Forces and moments

In applying the maximum stress criterion, the magnitude of the internal loads has been obtained. Note that the internal loads are defined with respect to the local frame. For estimates of the applied loads at $s = L$, which are defined in the fixed frame instead, the equilibrium equations of a finite beam segment can be used.

The relation between the internal moments at s and the applied moments at $s = L$ is given by

$$\begin{bmatrix} M_{\bar{x}}(s) \\ M_{\bar{y}}(s) \\ M_{\bar{z}}(s) \end{bmatrix} = \mathbf{R}^T \left\{ \begin{bmatrix} \bar{M}_x \\ \bar{M}_y \\ \bar{M}_z \end{bmatrix} + \left[\begin{bmatrix} L + u_x(L) \\ u_y(L) \\ u_z(L) \end{bmatrix} - \begin{bmatrix} s + u_x(s) \\ u_y(s) \\ u_z(s) \end{bmatrix} \right] \times \begin{bmatrix} \bar{F}_x \\ \bar{F}_y \\ \bar{F}_z \end{bmatrix} \right\} - \mathbf{f}_{\text{te}}(s). \quad (20)$$

With a second-order expansion of $\mathbf{R}^T$, it can be approximated by

$$\begin{bmatrix} M_{\bar{x}}(s) \\ M_{\bar{y}}(s) \\ M_{\bar{z}}(s) \end{bmatrix} \approx \begin{bmatrix} 1 - \phi_y^2/2 - \phi_z^2/2 & \phi_z & -\phi_y \\ -\phi_z + \phi_x\phi_y & 1 - \phi_x^2/2 - \phi_z^2/2 & \phi_x + \phi_y\phi_z \\ \phi_y + \phi_x\phi_z & -\phi_x & 1 - \phi_x^2/2 - \phi_y^2/2 \end{bmatrix} \times \left\{ \begin{bmatrix} \bar{M}_x \\ \bar{M}_y \\ \bar{M}_z \end{bmatrix} - \begin{bmatrix} \bar{F}_y \left[u_z(L) - u_z(s) \right] - \bar{F}_z \left[u_y(L) - u_y(s) \right] \\ \bar{F}_z \left[L + u_x(L) - s - u_x(s) \right] - \bar{F}_x \left[u_z(L) - u_z(s) \right] \\ \bar{F}_x \left[u_y(L) - u_y(s) \right] - \bar{F}_y \left[L + u_x(L) - s - u_x(s) \right] \end{bmatrix} \right\} - \mathbf{f}_{\text{te}}(s). \quad (21)$$

In Eq. (20), the symbol × represents the cross product; in Eq. (21), it represents the matrix–vector multiplication. Function $\mathbf{f}_{\text{te}}(s)$ is given by

$$\begin{bmatrix} I_{\text{te}} F_{\bar{x}}(s) \phi_x'(s) & 0 & 0 \end{bmatrix}^T \quad (22)$$

and represents the correction to the internal torsion moment $M_{\bar{x}}(s)$ because of the modification of the axial strain $\gamma_{\bar{x}}$ to account for the torsion–elongation coupling, as described in Section 2.1.2.

Similarly, it follows for the relation between the internal forces and applied forces at $s = L$ that

$$\begin{bmatrix} F_{\bar{x}}(s) \\ F_{\bar{y}}(s) \\ F_{\bar{z}}(s) \end{bmatrix} = \mathbf{R}^T \begin{bmatrix} \bar{F}_x \\ \bar{F}_y \\ \bar{F}_z \end{bmatrix}. \quad (23)$$

From these equations, it can be seen what the magnitude of the fixed-frame applied loads can maximally be, so as not to exceed the maximum-stress estimates of the local-frame internal loads. As an example, for $\bar{M}_y$ not to exceed the maximum-stress estimate of $M_{\bar{y}}(s)$, it can be of order EL^3u^5. However, for it not to exceed the maximum-stress estimate of $M_{\bar{x}}(s)$, it can only be of order EL^3u^6, due to the term $\phi_z \bar{M}_y$ in the equilibrium equation for $M_{\bar{x}}(s)$. With similar reasoning, the estimate for $\bar{M}_x$, $\bar{F}_y L$ and $\bar{M}_z$ is EL^3u^7. While the maximum-stress estimate for the loads $\bar{F}_x L$, $\bar{M}_y$ and $\bar{F}_z L$ is EL^3u^6, the buckling criterion (EL^3u^7) is more conservative and should therefore be used instead.

2.4.6. Shear deformation

With the magnitude estimates for the internal loads, it follows that the shear angles (see the constitutive relations of Eq. (9)) $F_{\bar{y}}/kGA$ and $F_{\bar{z}}/kGA$ have magnitudes u^5 and u^3, respectively. They are at least an order smaller than the estimates for the maximum rotation angles. So, when bending deformation is dominant, the effects of shear deformation can be ignored in the formulation of the current work. In case the sheet flexure is loaded by only a force $\bar{F}_z$, shear angle $\gamma_{\bar{z}}$ could be significant with respect to rotation angle ϕ_y. Therefore, shear deformation in only the $\bar{z}$-direction is included in this work. As a consequence of assuming that $\gamma_{\bar{y}} \approx 0$, the transverse displacement u_y and rotation ϕ_z are not independent, but related by $u_y' = \phi_z$.

2.5. Choice of interpolation functions

In using the Hellinger–Reissner variational principle to obtain an approximate solution, interpolation functions for the internal loads ($M_{\bar{x}}$, $M_{\bar{y}}$, $M_{\bar{z}}$, $F_{\bar{x}}$, $F_{\bar{y}}$, $F_{\bar{z}}$, B) and the associated displacement fields (ϕ_x, ϕ_y, ϕ_z, u_x, u_y, u_z) can be chosen. With the order of magnitude estimates of Section 2.4, the order of the leading terms in the integrand of P can be estimated; it can be seen that they are all of the order EL^2u^8. Given the exact expressions for the internal moments in Eq. (20) and curvatures in Eq. (5), we choose interpolation functions that consist of only the largest terms (i.e. of order EL^2u^8) in those expressions, meaning that terms in the integrand of P of the order EL^2u^9 and lower are neglected. The displacement fields are interpolated by the simplest polynomial that is in agreement with the boundary conditions and coincidentally the solution of the fully linearized problem.

Table 1
Summary of the order of magnitude estimates in terms of powers of u (Section 2.4.1).

External forces	$\bar{F}_x$	$\bar{F}_y$	$\bar{F}_z$	Displacements	u_x	u_y	u_z
EL^2	u^7	u^7	u^7	L	u^2	u	u^2
Internal forces	$F_{\bar{x}}(s)$	$F_{\bar{y}}(s)$	$F_{\bar{z}}(s)$	Rotations	ϕ_x	ϕ_y	ϕ_z
EL^2	u^5	u^7	u^5		u	u^2	u
External moments	$\bar{M}_x$	$\bar{M}_y$	$\bar{M}_z$	Curvatures	$\kappa_{\bar{x}}$	$\kappa_{\bar{y}}$	$\kappa_{\bar{z}}$
EL^3	u^7	u^7	u^7	$1/L$	u	u^3	u
Internal moments	$M_{\bar{x}}(s)$	$M_{\bar{y}}(s)$	$M_{\bar{z}}(s)$	Strains	$\gamma_{\bar{x}}$	$\gamma_{\bar{y}}$	$\gamma_{\bar{z}}$
EL^3	u^7	u^5	u^7		u^3	u^5	u^3

The load interpolation functions are then given by

$$\begin{aligned} M_{\bar{x}}(s) &= \tilde{M}_x + \tilde{F}_z \left[\tilde{u}_y - u_y(s) \right] + u_y'(s) \left[\tilde{M}_y - \tilde{F}_z(L - s) \right] - I_{\text{te}} \tilde{F}_x \phi_x'(s), \\ M_{\bar{y}}(s) &= \tilde{M}_y - \tilde{F}_z(L - s), \\ M_{\bar{z}}(s) &= \tilde{M}_z + \tilde{F}_y(L - s) - \tilde{F}_x \left[\tilde{u}_y - u_y(s) \right] - \phi_x(s) \left[\tilde{M}_y - \tilde{F}_z(L - s) \right], \\ F_{\bar{x}}(s) &= \tilde{F}_x, \\ F_{\bar{y}}(s) &= 0, \\ F_{\bar{z}}(s) &= \tilde{F}_z. \end{aligned} \quad (24)$$

Tilde superscripts denote the unknown coefficients. The leading terms in the curvature and strain expressions are

$$\begin{aligned} \kappa_{\bar{x}} &= \phi_x', \\ \kappa_{\bar{y}} &= \phi_y' + \phi_x\phi_z' \approx \phi_y' + \phi_x u_y'', \\ \kappa_{\bar{z}} &= \phi_z' \approx u_y'', \\ \gamma_{\bar{x}} &= u_x' - \phi_z \left(\phi_z/2 - u_y' \right) + I_{\text{te}} \phi_x'^2/2 \approx u_x' + u_y'^2/2 + I_{\text{te}} \phi_x'^2/2, \\ \gamma_{\bar{y}} &= 0, \\ \gamma_{\bar{z}} &= u_z' + \phi_y. \end{aligned} \quad (25)$$

The displacement interpolation functions ($\xi = s/L$) are

$$\begin{aligned} \phi_x(\xi) &= \tilde{\phi}_x \left(3\xi^2 - 2\xi^3 \right), \\ \phi_y(\xi) &= \frac{1}{1 + \boldsymbol{\Phi}} \tilde{u}_z/L \left(-6\xi + 6\xi^2 \right) + \frac{1}{1 + \boldsymbol{\Phi}} \tilde{\phi}_y \left(-2\xi + 3\xi^2 + \boldsymbol{\Phi}\xi \right), \\ u_x(\xi) &= \tilde{u}_x \xi, \\ u_y(\xi) &= \tilde{u}_y \left(3\xi^2 - 2\xi^3 \right) + L\tilde{\phi}_z \left(-\xi^2 + \xi^3 \right), \\ u_z(\xi) &= \frac{1}{1 + \boldsymbol{\Phi}} \tilde{u}_z \left(3\xi^2 - 2\xi^3 + \boldsymbol{\Phi}\xi \right) + \frac{1}{2 + 2\boldsymbol{\Phi}} L\tilde{\phi}_y \left(2\xi^2 - 2\xi^3 + \boldsymbol{\Phi}\xi - \boldsymbol{\Phi}\xi^2 \right), \end{aligned} \quad (26)$$

where $\boldsymbol{\Phi} = 12EI_y/(kGAL^2)$.

The load interpolation functions of Eq. (24) can be seen to take the deformed configuration of the beam into account. The loads that are associated with relatively low stiffness, i.e. the internal torsion moment $M_{\bar{x}}$ and bending moment $M_{\bar{z}}$, are dependent on the deformed shape of the sheet flexure as given by the displacement and rotation associated with relatively low stiffness, i.e. $u_y(s)$ and $\phi_x(s)$.

For an interpolation of the varying bimoment that is consistent with this approximation of the deformed sheet flexure configuration, we use the torsion ODE from Eq. (10) with the interpolation of the internal torsion moment $M_{\bar{x}}(s)$ from Eq. (24) in order to determine $\kappa_{\bar{x}}(s)$ given the constrained warping boundary conditions

$$\kappa_{\bar{x}}(0) = \kappa_{\bar{x}}(L) = 0. \quad (27)$$

In turn, the internal bimoment interpolation follows from the constitutive relation for $B(s)$, as given by Eq. (9). This way, the bimoment interpolation does not introduce additional unknown coefficients, which otherwise would need to be determined as well. The bimoment interpolation is a function of the same unknown coefficients as $M_{\tilde{x}}(s)$, which it is based on, and of the dimensionless parameter

$$\lambda = \sqrt{\frac{GJL^2}{EI_w}} \approx \sqrt{\frac{24}{1+\nu}}\frac{L}{w}. \tag{28}$$

This parameter can be regarded as a spatial decay rate for the warping constraint. The full expression is provided in Appendix A.2.

The interpolation functions clearly reflect that we consider the sheet flexure as an elastic constraint element with three DOFs and three support directions, as a principal consequence of the first assumption of Section 2.4.1 that the width is the same order as the length. It can be seen that the strain and curvature approximations of Eq. (25) in the support directions, i.e. $\kappa_{\tilde{y}}$ and $\gamma_{\tilde{x}}$, have a second-order term, whereas the strain and curvature approximations associated with the DOFs, i.e. $\kappa_{\tilde{x}}$ and $\kappa_{\tilde{z}}$, only have the linear term. Conversely, the load interpolation of Eq. (24) in the support directions, i.e. $F_{\tilde{x}}$, $M_{\tilde{y}}$ and $F_{\tilde{z}}$, only consists of the linear solution, whereas the load interpolation associated with the DOFs, i.e. $M_{\tilde{x}}$ and $M_{\tilde{z}}$, contains a coupling with the large displacements u_y and ϕ_x and the support direction loads $\tilde{F}_x$, $\tilde{M}_y$ and $\tilde{F}_z$ to take the deformed configuration into account.

2.6. Equation format

The interpolation functions of Eqs. (24) and (26) contain six unknown displacement (and rotation) coefficients and six unknown moment (and force) coefficients, whose equilibrium value can be obtained by application of the variational principle. Since the interpolation functions are based on physical insight, the notation of the superscript tilde serves to indicate that the coefficient is unknown while also showing what physical quantity the coefficient is based on. For instance, $\bar{F}_y$ is the actual applied force in the y-direction that does external work, while $\tilde{F}_y$ denotes a coefficient that is unknown and based on the physical force in the y-direction. A consequence of the physical basis for the interpolation functions is that the moment interpolation functions depend on both the moment coefficients and the displacement coefficients, as per the deformed-configuration equilibrium of Eq. (20). It is this physically-motivated coupling that enables the relatively low-order polynomials to capture the relevant higher-order energy terms, including some fourth-order energy terms that lead to the desired third-order elastokinematic terms in the final model equations.

Substitution of Eqs. (24) and (26) in the potential energy expression of Eq. (12) yields a polynomial scalar expression of the Hellinger–Reissner potential energy P, which can be used for further calculations. It is given in full in Appendix A.3. In addition to the 12 unknown coefficients denoted by a superscript tilde, the six loads $\bar{M}_x, \bar{M}_y, \bar{M}_z, \bar{F}_x, \bar{F}_y, \bar{F}_z$ applied at the free end are present.

Since the integrand of P_{int} in Eq. (13) is at most quadratic in the moment fields and the moment interpolation functions of Eq. (24) are linear in the moment coefficients, it follows that P is at most quadratic in the moment coefficients. Taking variations with respect to the moment coefficients then yields a linear system of equations (representing the compatibility equations) in the unknown moment coefficients, meaning that they can be determined. In principle, this solution could be used to eliminate the moment coefficients from P and reduce it to a standard potential energy formulation expressed in terms of only the displacement coefficients. While that does reduce the number of equations and unknown coefficients, it yields an energy scalar that is a rational function instead of a polynomial. We have found that some calculations are considerably easier to carry out with the larger polynomial, especially when they involve differentiation-type operations, even when using analytical solver software. This is elaborated on in Section 5 on the analysis of assemblies of multiple sheet flexures.

The distinction between the high and low stiffness deformation modes of a sheet flexure is also manifested in the structure of polynomial P. The terms accounting for the nonlinear behavior, i.e. the third- and fourth-order terms in P, are due to the coupling in the moment interpolation in Eq. (24) between loads and displacement, and due to the second-order terms in Eq. (25) for the strains and curvatures. Specifically, the coupling in the moment interpolation is between the support direction loads $\tilde{F}_x$, $\tilde{M}_y$, $\tilde{F}_z$ and the DOFs $\tilde{\phi}_x$, $\tilde{u}_y$ and $\tilde{\phi}_z$. The second-order terms for the strains and curvatures only involve the DOFs. Conversely, there is no nonlinear coupling between the loads in the directions of the DOFs, i.e. $\tilde{M}_x$, $\tilde{F}_y$, $\tilde{M}_z$, and the motion in the support directions, i.e. $\tilde{u}_x$, $\tilde{\phi}_y$ and $\tilde{u}_z$.

Because of this structure of the third- and fourth-order energy terms, the variations with respect to the six moment coefficients can be solved for the combination of $\tilde{M}_x$, $\tilde{F}_y$, $\tilde{M}_z$, $\tilde{u}_x$, $\tilde{\phi}_y$ and $\tilde{u}_z$ and used for eliminating $\tilde{M}_x$, $\tilde{F}_y$, $\tilde{M}_z$ from P, while retaining its polynomial structure. P then still depends on the six displacement coefficients, the three moment coefficients $\tilde{F}_x$, $\tilde{M}_y$ and $\tilde{F}_z$, in addition to the material parameters, geometry parameters and the six applied loads. This expression of P is used in the following sections.

It can be seen that the Hellinger–Reissner variational principle offers the advantage that the desired fourth-order energy terms consist of a mix of displacement and moment variables, which is at most quadratic in the displacement and the moment variables. It means that the process of taking variations then yields relatively simple equations that consist of at most third-order terms that are linear in either the displacement or the moment variables.

In line with the observation in Table 1 that the error motions $\tilde{u}_x$, $\tilde{\phi}_y$ and $\tilde{u}_z$ are an order smaller than the DOFs $\tilde{\phi}_x$, $\tilde{u}_y$ and $\tilde{\phi}_z$, we choose to express the model as functions of these three DOFs and the three loads in the other directions, further exploiting the distinction between the deformation modes of high and low stiffness. It means that the mathematical expressions of the model are a representation of the *actuation loads* $\bar{M}_x$, $\bar{F}_y$ and $\bar{M}_z$, and the *error motions* $\tilde{u}_x$, $\tilde{\phi}_y$ and $\tilde{u}_z$.

The closed-form solution can be obtained by first taking variations with respect to $\tilde{F}_x$, $\tilde{M}_y$ and $\tilde{F}_z$ and solving for the three error motions $\tilde{u}_x$, $\tilde{\phi}_y$ and $\tilde{u}_z$. Second, the variations of P with respect to the three error motions can be used to eliminate $\tilde{M}_x$, $\tilde{F}_y$ and $\tilde{M}_z$. Third, the moments dual to the Tait–Bryan angles can be transformed to moment vector components, according to Eq. (15). Fourth, the variations with respect to the DOFs $\tilde{\phi}_x$, $\tilde{u}_y$, $\tilde{\phi}_z$ can be solved for the actuation loads $\bar{M}_x$, $\bar{F}_y$ and $\bar{M}_z$. The particular choice of rotation order in Eq. (3) ensures that the transformation from $\bar{M}_y^{\text{TB}}$ to $\bar{M}_y$ in Eq. (15) is as simple as possible, so that the third and fourth step described here can be carried out with relative ease. The rotation order choice is immaterial to the accuracy of the resulting model and only relevant to the mathematical labor involved.

3. Results

The expressions that constitute the sheet flexure model are shown in a mixed compliance–stiffness matrix format. The three load–displacement relations are given by

$$\begin{aligned}\bar{M}_x = c_1\frac{GJ}{L}\tilde{\phi}_x &+ \bar{M}_y\begin{bmatrix}c_3 & c_4\end{bmatrix}\begin{bmatrix}\tilde{u}_y/L\\ \tilde{\phi}_z\end{bmatrix}\\ &+ \bar{F}_z L\begin{bmatrix}c_5 & c_6\end{bmatrix}\begin{bmatrix}\tilde{u}_y/L\\ \tilde{\phi}_z\end{bmatrix}\\ &+ c_2\bar{F}_x\frac{I_{\text{te}}}{L}\tilde{\phi}_x,\end{aligned} \tag{29}$$

$$\begin{aligned}\bar{F}_y = \frac{EI_z}{L^2}\begin{bmatrix}12 & -6\end{bmatrix}\begin{bmatrix}\tilde{u}_y/L\\ \tilde{\phi}_z\end{bmatrix} &+ \bar{F}_x\begin{bmatrix}6/5 & -1/10\end{bmatrix}\begin{bmatrix}\tilde{u}_y/L\\ \tilde{\phi}_z\end{bmatrix}\\ &+ c_3\bar{M}_y\tilde{\phi}_x/L + c_5\bar{F}_z\tilde{\phi}_x,\end{aligned} \tag{30}$$

$$\bar{M}_z = \frac{EI_z}{L}\begin{bmatrix}-6 & 4\end{bmatrix}\begin{bmatrix}\tilde{u}_y/L\\ \tilde{\phi}_z\end{bmatrix} + \bar{F}_x L\begin{bmatrix}-1/10 & 2/15\end{bmatrix}\begin{bmatrix}\tilde{u}_y/L\\ \tilde{\phi}_z\end{bmatrix} + (1+c_4)\bar{M}_y\tilde{\phi}_x + c_6\bar{F}_z L\tilde{\phi}_x. \quad (31)$$

These expression describe how the actuation loads depend on the applied loads and the DOFs. Besides the common terms from linear analysis, there are terms that depend on both the DOF and the applied load. As in the 2-D case, these capture load-stiffening (and load-softening) behavior [8]. The solution of the variational problem also yields terms in Eqs. (29)–(31) that are quadratic in the applied loads; these have been discarded at only a small error for parameter values in accordance with the earlier estimates. The coefficients c_i are functions of only the warping parameter λ and are given in Appendix A.4.

The error motion relations are given by

$$\begin{aligned}\tilde{u}_x/L = {} & \bar{F}_x\frac{1}{EA} \\ & + \begin{bmatrix}\tilde{\phi}_z & \tilde{u}_y/L\end{bmatrix}\begin{bmatrix}-1/15 & 1/20\\ 1/20 & -3/5\end{bmatrix}\begin{bmatrix}\tilde{\phi}_z\\ \tilde{u}_y/L\end{bmatrix} + c_7 I_{te}\tilde{\phi}_x^2/L^2 \\ & + \bar{F}_x\frac{L^2}{EI_z}\begin{bmatrix}\tilde{\phi}_z & \tilde{u}_y/L\end{bmatrix}\begin{bmatrix}11/6300 & -1/1400\\ -1/1400 & 1/700\end{bmatrix}\begin{bmatrix}\tilde{\phi}_z\\ \tilde{u}_y/L\end{bmatrix} \\ & + \bar{F}_x c_{11}\frac{I_{te}^2}{GJL^2}\tilde{\phi}_x^2 \\ & + \bar{M}_y\frac{L}{EI_z}\tilde{\phi}_x\left(-\frac{\tilde{u}_y}{700L} + \frac{\tilde{\phi}_z}{1400}\right) \\ & + \bar{M}_y\frac{I_{te}}{GJL}\tilde{\phi}_x\left(-c_{13}\tilde{\phi}_z - c_{11}\tilde{u}_y/L\right) \\ & + \bar{F}_z\frac{L^2}{EI_z}\tilde{\phi}_x\left(\frac{\tilde{u}_y}{1400L} - \frac{\tilde{\phi}_z}{300}\right) + \bar{F}_z\frac{I_{te}}{GJ}\tilde{\phi}_x\left(c_{18}\tilde{\phi}_z - c_{13}\tilde{u}_y/L\right),\end{aligned} \quad (32)$$

$$\begin{aligned}\tilde{\phi}_y = {} & -\frac{1}{2}\bar{F}_z\frac{L^2}{EI_y} + \bar{M}_y\frac{L}{EI_y} \\ & + (c_9-1)\tilde{\phi}_x\tilde{\phi}_z + c_8\tilde{\phi}_x\tilde{u}_y/L \\ & + \bar{F}_x\frac{L^2}{EI_z}\tilde{\phi}_x\left(-\frac{\tilde{u}_y}{700L} + \frac{\tilde{\phi}_z}{1400}\right) + \bar{F}_x\frac{I_{te}}{GJ}\tilde{\phi}_x\left(-c_{13}\tilde{\phi}_z - c_{11}\tilde{u}_y/L\right) \\ & + \bar{M}_y\frac{L}{GJ}\begin{bmatrix}\tilde{\phi}_z & \tilde{u}_y/L\end{bmatrix}\begin{bmatrix}c_{12} & c_{13}\\ c_{13} & c_{14}\end{bmatrix}\begin{bmatrix}\tilde{\phi}_z\\ \tilde{u}_y/L\end{bmatrix} + \bar{M}_y\frac{L}{EI_z}\frac{1}{700}\tilde{\phi}_x^2 \\ & + \bar{F}_z\frac{L^2}{GJ}\begin{bmatrix}\tilde{\phi}_z & \tilde{u}_y/L\end{bmatrix}\begin{bmatrix}c_{19} & c_{20}\\ c_{20} & c_{13}\end{bmatrix}\begin{bmatrix}\tilde{\phi}_z\\ \tilde{u}_y/L\end{bmatrix} - \bar{F}_z\frac{L^2}{EI_z}\frac{1}{1400}\tilde{\phi}_x^2,\end{aligned} \quad (33)$$

$$\begin{aligned}\tilde{u}_z/L = {} & \frac{1}{3}\bar{F}_z\frac{L^2}{EI_y} - \frac{1}{2}\bar{M}_y\frac{L}{EI_y} + \bar{F}_z\frac{1}{kGA} \\ & + c_{10}\tilde{\phi}_x\tilde{\phi}_z + c_9\tilde{\phi}_x\tilde{u}_y/L \\ & + \bar{F}_x\frac{I_{te}}{GJ}\tilde{\phi}_x\left(c_{18}\tilde{\phi}_z - c_{13}\tilde{u}_y/L\right) + \bar{F}_x\frac{L^2}{EI_z}\tilde{\phi}_x\left(\frac{\tilde{u}_y}{1400L} - \frac{\tilde{\phi}_z}{300}\right) \\ & + \bar{M}_y\frac{L}{GJ}\begin{bmatrix}\tilde{\phi}_z & \tilde{u}_y/L\end{bmatrix}\begin{bmatrix}c_{19} & c_{20}\\ c_{20} & c_{13}\end{bmatrix}\begin{bmatrix}\tilde{\phi}_z\\ \tilde{u}_y/L\end{bmatrix} - \bar{M}_y\frac{L}{EI_z}\frac{1}{1400}\tilde{\phi}_x^2 \\ & + \bar{F}_z\frac{L^2}{GJ}\begin{bmatrix}\tilde{\phi}_z & \tilde{u}_y/L\end{bmatrix}\begin{bmatrix}c_{15} & c_{16}\\ c_{16} & c_{17}\end{bmatrix}\begin{bmatrix}\tilde{\phi}_z\\ \tilde{u}_y/L\end{bmatrix} + \bar{F}_z\frac{L^2}{EI_z}\frac{43}{6300}\tilde{\phi}_x^2.\end{aligned} \quad (34)$$

These expressions describe how the error motions in the constraint directions depend on the applied loads and the DOFs. The model equations are available for download [27].

For the purpose of interpretation and verification of the model, Eqs. (29)–(34) are summarized as

$$\begin{bmatrix}\bar{M}_x\\ \bar{F}_y\\ \bar{M}_z\end{bmatrix} = \left[\mathbf{K}_1 + \mathbf{K}_2\left(\bar{F}_x, \bar{M}_y, \bar{F}_z\right)\right]\begin{bmatrix}\tilde{\phi}_x\\ \tilde{u}_y\\ \tilde{\phi}_z\end{bmatrix}, \quad (35)$$

$$\begin{bmatrix}\tilde{u}_x\\ \tilde{\phi}_y\\ \tilde{u}_z\end{bmatrix} = \left[\mathbf{C}_1 + \mathbf{C}_2\left(\tilde{\phi}_x, \tilde{u}_y, \tilde{\phi}_z\right)\right]\begin{bmatrix}\bar{F}_x\\ \bar{M}_y\\ \bar{F}_z\end{bmatrix} + \mathbf{p}_1\left(\tilde{\phi}_x, \tilde{u}_y, \tilde{\phi}_z\right) \quad (36)$$

to highlight the structure. The matrices $\mathbf{K}_1$ and $\mathbf{C}_1$ account for the common linear stiffness and compliance contributions. $\mathbf{K}_2$ is only linearly dependent on the applied loads and accounts for changes in the actuation stiffness due to applied loads, sometimes referred to as geometric load-stiffening and load-softening effects. Quadratic vector-function $\mathbf{p}_1$ captures a purely kinematic relation between the error motions and the DOFs; it describes an error motion incurred from motion in the DOFs. Matrix $\mathbf{C}_2$ is still a (quadratic) function of the DOFs and governs the decrease in support stiffness that accompanies motion in the DOFs. It is referred to as an elastokinematic effect in literature [8,10] and tends to limit the performance of large range of motion precision mechanisms consisting of sheet flexures. The terms associated with matrix $\mathbf{C}_2$ are *third-order* terms in the model variables, i.e. the DOFs and the applied loads. Matrix $\mathbf{C}_2$ can be considered a principal result of the current analysis: while the other terms in Eqs. (35)–(36) could be found with a less detailed analysis, $\mathbf{C}_2$ is only obtained when the fourth-order energy terms are considered. For this reason, the current model is referred to as a third-order stiffness formulation.

A consequence of the structure of Eqs. (35) and (36) is that the actuation stiffness is modeled as a quantity independent of the DOFs and the support stiffness independent of the applied loads.

4. Verification

4.1. Prior art

For a verification of the model described by Eqs. (29)–(34), we first note the relation with prior art. The planar beam constraint model considers a 2-D sheet flexure, which has DOFs $\tilde{\phi}_z$ and $\tilde{u}_y$, and applied load $\bar{F}_x$ [8]. The planar model constitutes two expressions for the actuation loads $\bar{F}_y$ and $\bar{M}_z$, and one expression for the error motion $\tilde{u}_x$. All of the terms in those expressions can be identified within the current spatial model. The same terms can be found in the expressions derived for 2-D sheet flexures that are subjected to axial loads large with respect to the critical load [28]. The expression for $\tilde{u}_z$ is the same as the one derived in the previous work on the lateral support stiffness of a sheet flexure when constrained warping can be disregarded and only $\tilde{u}_y$ is prescribed at the free end, i.e. setting $\bar{M}_x = \bar{M}_z = 0$ and leaving $\tilde{\phi}_x$ and $\tilde{\phi}_z$ free [12]. Also, parts of the expressions for $\tilde{\phi}_y$ and $\tilde{u}_z$ can be found in the earlier work on the error motions of 3-D sheet flexures that are limited in twist angle [13], when the effects of constrained warping present in the current model are disregarded.

While the model describes the change in stiffness due to applied loads, see $\mathbf{K}_2$ in Eq. (35), the buckling load in general is not predicted with sufficient accuracy. This matches the assumptions in Section 2.4: the applied loads are assumed to be an order of magnitude smaller than the critical load. For specific boundary conditions, though, the critical load prediction may be found to be accurate, such as for the case of torsional buckling due to $\bar{F}_x$ with $\tilde{u}_y = \tilde{\phi}_z = 0$ or the case of axial buckling due to $\bar{F}_x$ with $\tilde{\phi}_z = 0$. For these cases, it appears that the assumed displacement field is a sufficiently accurate representation of the corresponding buckling mode. An example of the specific use of the buckling modes of a system for refining the interpolation and obtaining accurate predictions of the critical load can be found in Ref. [29].

Bai et al. [11] have developed a 3-D beam model that assumes bending curvatures $\kappa_{\bar{y}}$ and $\kappa_{\bar{z}}$ of equal magnitude, whereas the assumptions in Section 2.4 of the current work imply that $\kappa_{\bar{z}} \gg \kappa_{\bar{y}}$ for what we consider a typical sheet flexure constraint element. As a consequence, the model of Bai et al. does not discriminate between a bending plane for high and for low stiffness; $\tilde{u}_z$ is not necessarily a constraint direction and $\tilde{\phi}_y$ and $\tilde{u}_z$ are not necessarily error motions; their model therefore captures e.g. the effect of large $\tilde{u}_z$ and $\tilde{\phi}_y$ on $\tilde{u}_x$ as parasitic motion, unlike the current work. The essential difference between the two

models lies in the allowable values for w/L. For the model of Bai et al. w/L should remain small since torsion-elongation (Wagner) coupling, constrained warping and shear deformation have not been included and all become significant when $w \to L$. These effects are considered in the current work.

4.2. Verification procedure

To facilitate the verification of the model, which could be regarded as a 6 × 6 system of nonlinear stiffness relations with 21 unique components, the equation structure represented by Eqs. (35)–(36) can be utilized: by first establishing the validity of the structure for the parameter range of interest, only the accuracy of the function $\mathbf{p}_1$ and the unique components of $\mathbf{K}_2$ and $\mathbf{C}_2$ need to be verified.

For the comparison with finite element analysis, a model in ANSYS Mechanical (with two-node BEAM188 and four-node SHELL181 elements) and SPACAR (with two-node BEAMW elements) is used with all nonlinear analysis options enabled [30–32]. The parameter values are based on the order of magnitude estimates of Section 2.4 for a sheet flexure with a length of 100 mm. Table 2 lists the corresponding dimensions, material properties and maximum values for the applied loads and DOFs. The equilibrium configuration in both programs is determined for various combinations of the applied loads and DOFs. By means of an additional perturbation analysis, the stiffness matrix at the free end in the deformed configuration can be calculated and cast into the mixed format

$$\begin{bmatrix} \Delta\bar{M}_x \\ \Delta\bar{F}_y \\ \Delta\bar{M}_z \\ \Delta\tilde{u}_x \\ \Delta\tilde{\phi}_y \\ \Delta\tilde{u}_z \end{bmatrix} = \mathbf{B} \begin{bmatrix} \Delta\bar{F}_x \\ \Delta\bar{M}_y \\ \Delta\bar{F}_z \\ \Delta\tilde{\phi}_x \\ \Delta\tilde{u}_y \\ \Delta\tilde{\phi}_z \end{bmatrix} \tag{37}$$

so that the numerical entries of matrix $\mathbf{B}$ can be compared with the components of $\mathbf{K}_1$, $\mathbf{K}_2$, $\mathbf{C}_1$ and $\mathbf{C}_2$.

4.3. Equation structure validity

To test the linear relationship between the actuation loads and the DOFs that Eq. (35) portrays, the ANSYS model with plate elements is loaded by the maximum values from Section 2.4 for all applied loads simultaneously. The three actuation loads are observed as the three DOFs are incremented individually to their maximum values. It is found that the maximum relative error with respect to a least squares fit of a linear function is at most 0.7% for eight of the nine cases. The only significant deviation is observed for the torsion moment $\bar{M}_x$ as a function of the torsion angle $\tilde{\phi}_x$. With increasing $\tilde{\phi}_x$, the Wagner torque [33],

$$\frac{1}{360} E w^5 t \left(\phi'_x\right)^3, \tag{38}$$

which is a nonlinear function of the specific twist angle acting as a stiffening effect, starts to dominate the response: the deviation is 10% for 0.05 rad and 34% for 0.1 rad. Note that this Wagner torque is different from the Wagner term (the torsion–elongation coupling), which is taken into account by $\gamma_{\bar{x}}$ in Section 2.1.2. The Wagner torque depends strongly on the sheet flexure width and is not captured by the used beam-based finite elements (which predict a linear response that is in agreement with the current analytical model). The torque could readily be incorporated into the model expression for $\bar{M}_x$ by accounting for the associated strain energy per unit length term [34]

$$\frac{1}{1440} E w^5 t \kappa_{\bar{x}}^4 \tag{39}$$

in P_{int} in Eq. (13). The additional term in $\bar{M}_x$ is then found to be

$$\frac{1}{175} E w^5 t \tilde{\phi}_x{}^3 / L^3. \tag{40}$$

Table 2
Verification parameters: dimensions, material properties, and maximum values for the applied loads and DOFs.

L [mm]	w [mm]	t [mm]	E [GPa]	ν [–]	
100	100	2.25	200	0.3	
$\bar{F}_x$ [kN]	$\bar{M}_y$ [N m]	$\bar{F}_z$ [kN]	$\tilde{\phi}_x$ [–]	$\tilde{u}_y$ [mm]	$\tilde{\phi}_z$ [–]
3.42	342	3.42	0.15	15	0.15

It can be seen that this term has less than 10% effect on the expression for $\bar{M}_x$ e.g. when w/L is reduced to 0.5 and the torsion angle $\tilde{\phi}_x = 0.15$ rad or when w/L stays 1 but $\tilde{\phi}_x < 0.03$ rad.

The Wagner torque also has an effect on the error motions. Capturing this analytically is considerably more involved because of the interplay with the nonuniform torsion (warping) in the deformed configuration. The additional term of Eq. (38) renders the differential equation Eq. (10) nonlinear. It is unlikely that the increased complexity of the bimoment or torsion moment interpolation that the inclusion in the variational framework would require can be captured in the compact format of the current formulation. Additionally, since the effect is clearly identifiable, and much less pronounced in sheet flexures with smaller width-to-length ratios, omission in the model is deemed acceptable. With a numerical element implementation of this formulation, the effect of the Wagner torque on the error motions can be captured by simply accounting for Eq. (40) in the element description and using multiple elements to model a sheet flexure [35].

4.4. Model accuracy

Since the presented model is an approximation based on beam theory, errors are incurred in two stages. These can be identified by comparing against

- beam finite elements, to assess the accuracy of the approximation (consisting of interpolation and truncation),
- plate (shell) finite elements, to expose relevant effects outside beam theory and assess the validity of the use of beam theory.

Due to the large width-to-length ratio of some sheet flexures, beam theory may not be able to capture all relevant effects. Besides the mentioned Wagner torque, two facets of anticlastic curvature play a role. Primarily, the anticlastic curvature of the cross-section manifests itself as a bending stiffness that increases with bending deformation, dependent on the ratio $w^2/(Rt)$, where R is the bending radius [36]. In the limit case of plane strain, the bending stiffness increases by a factor of $1/(1-\nu^2)$. For sheet flexures, the common physical embodiment of the interfaces at the two ends (e.g. clamping blocks) prevents the local anticlastic curvature, leading to an increase in actuation stiffness $\mathbf{K}_1$ that is present even for infinitesimal deformation and dependent on the ratio w/L [37].

For the verification of the symmetric matrix $\mathbf{K}_1+\mathbf{K}_2$, the deviation of the six unique components with respect to the shell elements in ANSYS is depicted in Fig. 4 for increasing values of the three applied loads (and zero values of the DOFs). It can be seen that the deviation of the derivatives with respect to $\bar{F}_y$ and $\bar{M}_z$ is at most 7.8%, whereas the deviation of the derivatives with respect to $\bar{M}_x$ is at most 5.1%. This difference is already present for zero applied load and can be attributed to the effect of constrained anticlastic curvature: the deviation reduces to only 1.6% at most when the model is compared to the geometrically nonlinear beam element in ANSYS and SPACAR, which does not model anticlastic curvature but does capture the load-stiffening effect of $\mathbf{K}_2$. In case the effect of anticlastic curvature is of interest, it could be taken into account by means of a modification of $\mathbf{K}_1$ according to the procedure of Meijaard [37].

For the verification of the symmetric matrix $\mathbf{C}_1 + \mathbf{C}_2$, we first note that $\mathbf{C}_2$ is a quadratic function of the three DOFs. Out of the various possible combinations of the DOFs, some interesting cases are

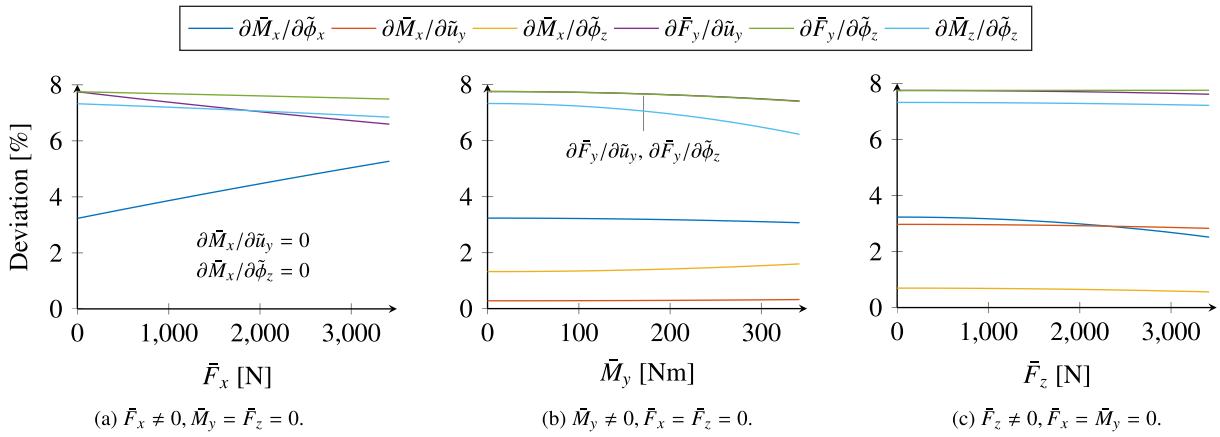

(a) $\bar{F}_x \neq 0, \bar{M}_y = \bar{F}_z = 0$. (b) $\bar{M}_y \neq 0, \bar{F}_x = \bar{F}_z = 0$. (c) $\bar{F}_z \neq 0, \bar{F}_x = \bar{M}_y = 0$.

Fig. 4. Deviation of the actuation load derivatives with respect to nonlinear ANSYS shell elements.

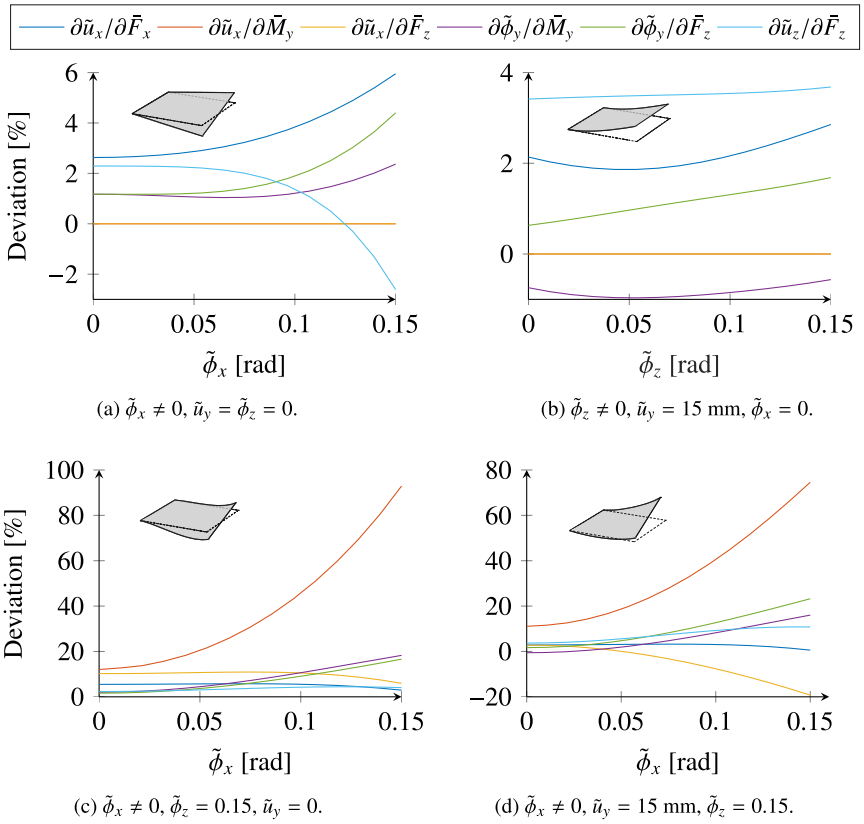

(a) $\tilde{\phi}_x \neq 0, \tilde{u}_y = \tilde{\phi}_z = 0$. (b) $\tilde{\phi}_z \neq 0, \tilde{u}_y = 15$ mm, $\tilde{\phi}_x = 0$.

(c) $\tilde{\phi}_x \neq 0, \tilde{\phi}_z = 0.15, \tilde{u}_y = 0$. (d) $\tilde{\phi}_x \neq 0, \tilde{u}_y = 15$ mm, $\tilde{\phi}_z = 0.15$.

Fig. 5. Deviation of the error motion derivatives with respect to nonlinear ANSYS shell elements. Small inset figures in the graphs represent the load cases visually. The larger deviations for $\partial\tilde{u}_x/\partial\bar{M}_y$ are mainly due to omission of the Wagner torque and strongly dependent on the width-to-length ratio of the sheet flexure. When the Wagner torque can be ignored, as is discussed in Section 4.4, the deviations for all graphs stay within 7.8%.

1. a nonzero $\tilde{\phi}_x$ only,
2. nonzero $\tilde{u}_y$ and $\tilde{\phi}_z$ only (the planar case),
3. a combination of $\tilde{\phi}_x$ and nonzero $\tilde{u}_y$ or $\tilde{\phi}_z$, and
4. combined nonzero values for all three DOFs.

Fig. 5 shows the deviation of the six unique components for these four cases with respect to shell elements. When only $\tilde{\phi}_x \neq 0$ (Fig. 5a), the maximum deviation is 6.0% and occurs at the maximum value of the twist angle $\tilde{\phi}_x$. In the planar case, Fig. 5b, the maximum deviation is 3.7%. In Fig. 5c, when $\tilde{\phi}_z$ is fixed to a nonzero value, it is observed that the deviation of the derivative $\partial\tilde{u}_x/\partial\bar{M}_y$ starts from a value of 13% and increases strongly with $\tilde{\phi}_x$. A similar trend is observed in the derivatives $\partial\tilde{\phi}_y/\partial\bar{M}_y$ and $\partial\tilde{\phi}_y/\partial\bar{F}_z$, although the deviation remains limited to 18% at the maximum twist angle. This is explained by the torsion moment needed in this case: the Wagner torque is dominant for the larger $\tilde{\phi}_x$ and is not included in the analytical model. When additionally $\tilde{u}_y = 15$ mm (Fig. 5d), the qualitative behavior is the same; up to $\tilde{\phi}_x = 0.1$ rad, the maximum deviation is 12%, except for $\partial\tilde{u}_x/\partial\bar{M}_y$. To exclude the effect of the Wagner torque, a comparison with beam elements shows that for the four cases the maximum deviation is only 3.7% for all derivatives, except $\partial\tilde{u}_x/\partial\bar{M}_y$ and $\partial\tilde{u}_x/\partial\bar{F}_z$: those two have a maximum deviation of 7.8%. Also, when shell elements are used and the width of the sheet flexure is reduced to $3L/4$, the deviations of $\partial\tilde{u}_x/\partial\bar{M}_y$ for the third and fourth case are already 48% and 22% smaller, respectively. The Wagner torque has less than 5% effect on the error motions when the width is

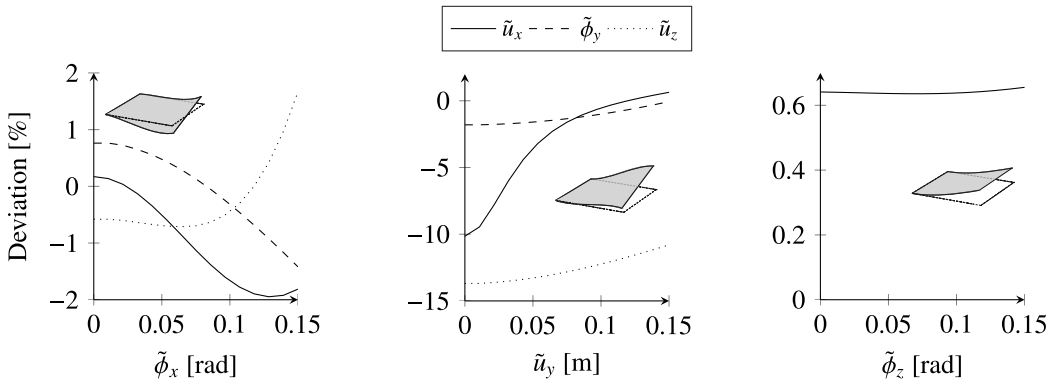

(a) $\tilde{\phi}_x \neq 0, \tilde{\phi}_z = 0.15, \tilde{u}_y = 0.$ (b) $\tilde{u}_y \neq 0, \tilde{\phi}_x = 0.15, \tilde{\phi}_z = 0.$ (c) $\tilde{\phi}_z \neq 0, \tilde{u}_y = 15$ mm, $\tilde{\phi}_x = 0.$

Fig. 6. Deviation of the error motions with respect to nonlinear ANSYS shell elements. Small inset figures in the graphs represent the load cases visually.

less than $L/3$. If the torsion angle is limited to 0.1 rad, the Wagner torque has already less than 5% effect when the width is $L/2$.

For the verification of the quadratic vector-valued function $\mathbf{p}_1$, the deviation of the error motions themselves with respect to ANSYS shell elements is depicted in Fig. 6 for various combinations of the DOFs. For the two cases of Figs. 6a and 6c, the maximum deviation is only 1.9%. When $\tilde{u}_y$ is incremented at a constant $\tilde{\phi}_x = 0.15$ (as shown in Fig. 6b), the maximum deviation is 14%. When compared with beam elements, the maximum deviation for all cases is only 0.1%.

The verification of the individual components of $\mathbf{K}_2$ and $\mathbf{C}_2$ for various load cases is sensitive and exposes deviations easily. The close match with the solution obtained with numerical beam elements indicates that the geometrically nonlinear effects within beam theory are described accurately by the model. From the comparison with shell elements, we conclude that the beam-based analytical model performs well, when the Wagner torque and, to a lesser extent, the anticlastic curvature can be disregarded. This is the case when mainly the DOFs $\tilde{u}_y$ and $\tilde{\phi}_z$ are used and the torsion angle $\tilde{\phi}_x$ remains limited. It helps that the Wagner torque actually leads to a higher support stiffness or at least a smaller decrease in support stiffness with DOF motion. This means that the current model only underestimates the support stiffness at the larger torsion angles. For precision applications that commonly demand a large value of support stiffness, the Wagner torque actually leads to a desired stiffening effect. Moreover, since the effect is clearly identifiable and much less pronounced for smaller width-to-length ratios, omission in the model is deemed acceptable. In case the torsion angle is large and the quantitative effect on the torsion moment or the support stiffness is desired, it should be modeled numerically [35].

5. Assemblies of sheet flexures

The variational principle used for deriving the spatial sheet flexure model can readily be applied to assemblies of sheet flexures. The procedure is to formulate the total potential energy of the system, take into account the kinematic constraints, take variations with respect to the unknowns, and solve the system for the parameters of interest. In general, when all sheet flexures are connected in parallel (rather than in series), meaning that both ends of all sheet flexures are connected to either the fixed world or a rigid frame, closed-form models can be obtained with the procedure demonstrated in this section. This is illustrated by the cases of a parallelogram flexure mechanism and a cross-hinge flexure mechanism, which both consist of two identical sheet flexures, as shown in Figs. 7 and 8.

The total potential energy in both cases is given by

$$P^{\text{tot}} = P^{\text{l}} + P^{\text{r}} - W^{\text{e}}, \tag{41}$$

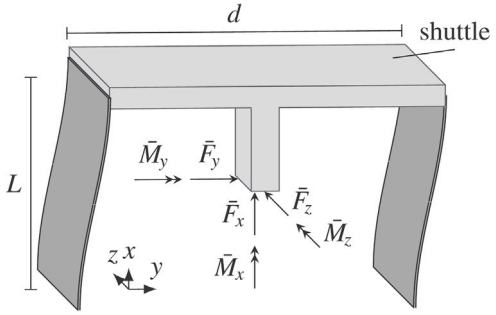

Fig. 7. Parallelogram flexure mechanism; loads are applied in the center of compliance. The w/L ratio of the sheet flexures is depicted smaller than simulated.

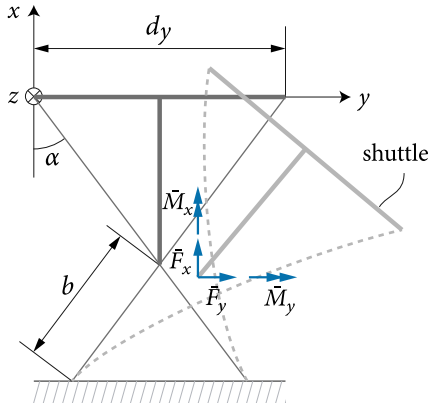

Fig. 8. Cross-hinge flexure mechanism; loads are applied in the center of compliance. Force $\bar{F}_z$ and moment $\bar{M}_z$ along the positive z-axis are not shown.

where the superscripts l and r denote the left and right sheet flexure, respectively. The external work W^{e} is due to loads that are applied in the center of compliance of the mechanism, and given by

$$\bar{M}_x^{\text{TB}}\phi_x^{\text{c}} + \bar{M}_y^{\text{TB}}\phi_y^{\text{c}} + \bar{M}_z^{\text{TB}}\phi_z^{\text{c}} + \bar{F}_x u_x^{\text{c}} + \bar{F}_y u_y^{\text{c}} + \bar{F}_z u_z^{\text{c}}. \tag{42}$$

The superscript c is used to denote displacements and rotations of the compliance center, resolved in the global frame. The superscripts TB are used to refer to moments that are dual to the Tait–Bryan angles, as discussed near Eq. (15). In principle, P denotes the expression of the potential energy of the sheet flexure that is given by P_{int} from Eq. (13). The full scalar polynomial presented in Eq. (A.12), without the external work due to the applied forces, can be used, although it is computationally easier if the polynomial is reduced by eliminating

three of the six moment coefficients as described in Section 2.6. Then, P is dependent on the six rotation and displacement coefficients (as in a conventional displacement-based potential energy formulation) and, as a consequence of the Hellinger–Reissner formulation, only three additional internal force and moment coefficients for each sheet flexure, which need to be solved for and ultimately eliminated.

The shuttle imposes kinematic constraints on the two sheet flexure ends, as derived in Appendix A.5. In terms of the coordinates of the compliance center, the translational kinematic constraints are given by

$$\begin{bmatrix} -h_x \\ d_y/2 \\ h_z \end{bmatrix} + \begin{bmatrix} u_x^c \\ u_y^c \\ u_z^c \end{bmatrix} - \mathbf{R}^s \begin{bmatrix} -h_x \\ d_y/2 \\ h_z \end{bmatrix} - \mathbf{R}^i \begin{bmatrix} u_x^l \\ u_y^l \\ u_z^l \end{bmatrix} = \begin{bmatrix} 0 \\ 0 \\ 0 \end{bmatrix}, \tag{43}$$

$$\begin{bmatrix} -h_x \\ -d_y/2 \\ -h_z \end{bmatrix} + \begin{bmatrix} u_x^c \\ u_y^c \\ u_z^c \end{bmatrix} - \mathbf{R}^s \begin{bmatrix} -h_x \\ -d_y/2 \\ -h_z \end{bmatrix} - \left(\mathbf{R}^i\right)^T \begin{bmatrix} u_x^r \\ u_y^r \\ u_z^r \end{bmatrix} = \begin{bmatrix} 0 \\ 0 \\ 0 \end{bmatrix}. \tag{44}$$

Parameter d_y denotes the shuttle length, and h_x and h_z the location of the center of compliance (as detailed in Appendix A.5). Rotation matrix $\mathbf{R}^i$ rotates the global frame about the z-axis to the frame attached to the undeformed sheet flexure. It is given by

$$\begin{bmatrix} \cos\alpha & \sin\alpha & 0 \\ -\sin\alpha & \cos\alpha & 0 \\ 0 & 0 & 1 \end{bmatrix} \tag{45}$$

and reduces to the identity matrix in the case of the parallelogram flexure mechanism, for which $\alpha = 0$. The rotational kinematic constraints due to the shuttle, expressed in terms of the coordinates of the compliance center, are given by

$$\mathbf{R}^s = \mathbf{R}^i \mathbf{R}^l \left(\mathbf{R}^i\right)^T \quad \text{and} \quad \mathbf{R}^s = \left(\mathbf{R}^i\right)^T \mathbf{R}^r \mathbf{R}^i. \tag{46}$$

Rotation matrices $\mathbf{R}^s$, $\mathbf{R}^l$ and $\mathbf{R}^r$ are given by $\mathbf{R}(s)$ from Eq. (3). $\mathbf{R}^s$ is parametrized by ϕ_x^c, ϕ_y^c and ϕ_z^c. Eqs. (43)–(46) can be solved for the displacements and rotations at the two sheet flexure ends. These relations can then be used to eliminate the sheet flexure displacements and rotations from P^{tot}, so that P^{tot} only depends on the six coordinates of the shuttle and the three additional Hellinger–Reissner internal load parameters per sheet flexure. For simplicity, the torsion–elongation coupling is ignored in this section.

Application of the Hellinger–Reissner principle to P^{tot} yields 12 algebraic equations for the 12 unknown coefficients. The six loads acting in the center of compliance, i.e. $\bar{F}_x$, $\bar{F}_y$, $\bar{F}_z$, $\bar{M}_x^{\text{TB}}$, $\bar{M}_y^{\text{TB}}$, $\bar{M}_z^{\text{TB}}$, are additional parameters in this system of equations. At this stage, the transformation of the moments, detailed in Section 2.3 near Eq. (15), can be performed. In line with the equation format for the sheet flexure, we choose to solve this system in terms of the DOFs and the loads applied in the five constraint directions. An adequate asymptotic solution can be obtained as a truncated series, since the exact solution of this system of equation requires considerable mathematical labor (even with analytical solver software), the added value of an exact solution is limited in the context of approximate theories such as the present beam theory, and the truncation of the series expansion can be physically motivated. By means of successive implicit differentiation of the 12 algebraic governing equations, recursive equations linear in the derivatives can be obtained for an arbitrary order and used to construct a series approximation. Since we choose to format the equations of the model such that smaller quantities (the error motions and actuation loads) are expressed as functions of larger quantities (the applied loads and, in particular, the DOFs), convergence of the series is less unlikely.

5.1. Parallelogram mechanism

For the parallelogram flexure mechanism, angle $\alpha = 0$, shuttle length $d_y = d$, and the location of the compliance center is given by $h_x = L/2$ and $h_z = 0$. The single displacement u_y^c is the DOF. By carrying out the implicit differentiation to the third order, simplifying terms by discarding EI_z and GJ with respect to $kGAL^2$ and EAL^2, neglecting third-order terms in a single variable, and constructing the series, the expression for the actuation force is obtained as

$$\bar{F}_y = u_y^c \left(\frac{24EI_z}{L^3} + \frac{6}{5L}\bar{F}_x \right). \tag{47}$$

The error motions in the five constraint directions are obtained as

$$u_x^c/L = \bar{F}_x \left(\frac{1}{2EA} + \frac{1}{1400EI_z} \left(u_y^c\right)^2 \right) - \frac{3}{5L^2} \left(u_y^c\right)^2, \tag{48}$$

$$u_z^c/L = \bar{F}_z \left(\frac{1}{2kGA} + \frac{L^2}{24EI_y} + \frac{p_1}{56GJ} \left(u_y^c\right)^2 \right), \tag{49}$$

$$\phi_x^c = \bar{M}_x \frac{L}{d^2} \left(\frac{2}{kGA} + \frac{L^2}{6EI_y} + \frac{p_1}{14GJ} \left(u_y^c\right)^2 \right), \tag{50}$$

$$\phi_y^c = \bar{M}_y/L \left(\frac{L^2}{2EI_y} + \frac{p_2}{10GJ} \left(u_y^c\right)^2 \right), \tag{51}$$

$$\phi_z^c = \bar{M}_z \frac{L}{d^2} \left(\frac{2}{EA} + \frac{1}{350EI_z} \left(u_y^c\right)^2 \right), \tag{52}$$

where coefficients p_1 and p_2 are related to the warping properties of the sheet flexures. The coefficients are trigonometric functions of λ only and provided in full in Appendix A.6. Convenient approximations are given by

$$p_1 = -0.0845 + 0.0493\lambda - 0.00114\lambda^2 + 0.0000101\lambda^3, \tag{53}$$

$$p_2 = -0.134 + 0.0627\lambda - 0.00160\lambda^2 + 0.0000151\lambda^3, \tag{54}$$

with at most a 2.4% deviation for $4.3 \le \lambda \le 43$, which corresponds with $1 \le L/w \le 10$ when $\nu = 0.3$.

The error motions u_z^c, ϕ_x^c and ϕ_y^c are the result of the spatial character of this analysis and ignored in a planar analysis. The expressions have the common constant stiffness term. In addition, they also have a contribution due to torsion, quadratically dependent on the degree of freedom u_y^c and referred to as an elastokinematic effect. It is this term that describes the observed increase in error motion, when the mechanism deflects in its DOF under a constant applied $\bar{F}_z$, $\bar{M}_x$ or $\bar{M}_y$ load. As a corollary, this term quantifies how the support stiffness $\mathrm{d}\bar{F}_z/\mathrm{d}u_z^c$, $\mathrm{d}\bar{M}_x/\mathrm{d}\phi_x^c$ and $\mathrm{d}\bar{M}_y/\mathrm{d}\phi_y^c$ decreases over the range of motion of the mechanism. When the error motion or support stiffness in these directions is relevant, it is likely that sheet flexures with large w/L ratios are used, as it tends to reduce the error motion and increase the support stiffness. When w/L is large, accurate modeling of the elastokinematic effect due to torsion requires the treatment of constrained warping that the current model provides.

As a verification by means of literature, we note that van Eijk has used the iterative–analytical approach to derive the expressions for $\bar{F}_y$ and u_x^c, and the spatial error motions ϕ_y^c and u_z^c (including constrained warping) [15]. The expression for u_x^c has been experimentally validated. Brouwer et al. have also derived the expressions for ϕ_y^c and u_z^c, though by means of a derivation specific to only the parallelogram flexure mechanism (unlike the current general derivation) [14]. They have validated the expressions extensively against FEM with a maximum deviation of 6.0% for $u_y^c = 0.1L$. Nijenhuis et al. have derived the expression for error motion u_z^c in Eq. (49) by means of a finite element-based discretization and provided an experimental validation [12].

Error motion u_x^c exhibits a structure similar to u_z^c and ϕ_y^c, but also includes a term independent of load $\bar{F}_x$; it is a purely kinematic contribution to displacement u_x^c, also referred to as a shortening effect [38]. Actuation load $\bar{F}_y$ has a term linear in $\bar{F}_x$, which describes the change in actuation stiffness due to applied load $\bar{F}_x$. The expressions for u_x^c, ϕ_z^c and $\bar{F}_y$ are not dependent on the out-of-plane parameters $\bar{M}_x$, $\bar{F}_z$ or $\bar{M}_y$. The fact that the current spatial analysis has resulted in these expressions implies that spatial effects have no significant contribution to u_x^c, ϕ_z^c and $\bar{F}_y$ and that a planar analysis would suffice. In fact, these terms have been derived before in earlier work on the planar analysis of the parallelogram flexure mechanism [8,39].

For a verification by means of a numerical simulation, a SPACAR model of the parallelogram mechanism with BEAMW elements is used.

Since these elements are beam-based, missing effects due to non-beam-like behavior are not revealed. These have been elaborated on in Section 4. This verification only serves to demonstrate the accuracy of the approximation of the geometrically nonlinear effects within beam theory. Similar to Eq. (37) for the single sheet flexure, the numerical compliance matrix in the deformed configuration is cast into the mixed format

$$\begin{bmatrix} \Delta\bar{F}_y \\ \Delta u_x^c \\ \Delta u_z^c \\ \Delta\phi_x^c \\ \Delta\phi_y^c \\ \Delta\phi_z^c \end{bmatrix} = \mathbf{B} \begin{bmatrix} \Delta u_y^c \\ \Delta\bar{F}_x \\ \Delta\bar{F}_z \\ \Delta\bar{M}_x \\ \Delta\bar{M}_y \\ \Delta\bar{M}_z \end{bmatrix}, \tag{55}$$

consistent with the format of the model equations in Eqs. (47)–(52). The equations provide the diagonal components of $\mathbf{B}$, which are dependent on the single DOF u_y^c. For the sheet flexure dimensions and material according to Table 2 and a shuttle length of 100 mm (equal to the sheet flexure length), the largest deviation between the SPACAR model and the analytical solution is 5.9% when $u_y^c = 0.15L$. When the width is reduced and $L = 100$ mm, $w = 25$ mm, $t = 0.3$ mm and $u_y^c = 0.1L$, the largest deviation is 2.4%. Even though $L/w = 4$ is now larger than one, the effect of constrained warping is still considerable: when free warping end-conditions are used in the SPACAR model (as if warping deformation were disregarded), compared with constrained warping conditions in the analytical model, the deviation in the components $\mathbf{B}_{3,3}$, $\mathbf{B}_{4,4}$, and $\mathbf{B}_{5,5}$ is still at least 41%.

5.2. Cross-hinge mechanism

For the cross-hinge mechanism of Fig. 8, we set the shuttle length d_y to

$$2L(1 - b/L)\sin\alpha \tag{56}$$

in order to introduce the dimensionless crossing length b/L as a parameter. The location of the compliance center is given by

$$h_x = L(1 - b/L)\cos\alpha, \quad h_z = w/2. \tag{57}$$

The single rotation ϕ_z^c of the compliance center is the DOF. Compared with the parallelogram mechanism, the mathematical labor for obtaining an asymptotic solution to the third order is considerably more involved because of the additional geometric parameters α and b/L. Unless the analytical sensitivities with respect to α and b/L are desired, it is recommended to choose values for α and b/L before carrying out the implicit differentiation.

For a doubly symmetric cross-hinge mechanism with $\alpha = 45°$ and $b = L/2$, the process of implicit differentiation, series construction, and simplification of small terms yields the expressions for the actuation load

$$\bar{M}_z = \phi_z^c \left(\frac{2EI_z}{L} - \frac{L}{3\sqrt{2}}\bar{F}_x \right), \tag{58}$$

the planar error motions

$$u_x^c/L = \bar{F}_x \left(\frac{1}{EA} + \frac{h_z^2}{EI_y} + \frac{L^2}{720EI_z}\left(\phi_z^c\right)^2 + \frac{h_z^2 p_3}{12GJ}\left(\phi_z^c\right)^2 \right) + \bar{M}_x \left(\frac{h_z}{EI_y} + \frac{h_z p_3}{12GJ}\left(\phi_z^c\right)^2 \right) + \frac{1}{6\sqrt{2}}\left(\phi_z^c\right)^2, \tag{59}$$

$$u_y^c/L = \bar{F}_y \left(\frac{1}{EA} + \frac{h_z^2}{EI_y} + \frac{L^2}{720EI_z}\left(\phi_z^c\right)^2 + \frac{h_z^2 p_3}{12GJ}\left(\phi_z^c\right)^2 \right) - \bar{M}_y \left(\frac{h_z}{EI_y} + \frac{h_z p_3}{12GJ}\left(\phi_z^c\right)^2 \right), \tag{60}$$

and the spatial error motions

$$u_z^c/L = \bar{F}_z \left(\frac{1}{2kGA} + \frac{L^2}{24EI_y} + \frac{L^2 p_2}{1440GJ}\left(\phi_z^c\right)^2 \right), \tag{61}$$

$$\phi_x^c = \bar{M}_x \left(\frac{L}{EI_y} + \frac{Lp_3}{12GJ}\left(\phi_z^c\right)^2 \right) + \bar{F}_x h_z \left(\frac{L}{EI_y} + \frac{Lp_3}{12GJ}\left(\phi_z^c\right)^2 \right), \tag{62}$$

$$\phi_y^c = \bar{M}_y \left(\frac{L}{EI_y} + \frac{Lp_3}{12GJ}\left(\phi_z^c\right)^2 \right) - \bar{F}_y h_z \left(\frac{L}{EI_y} + \frac{Lp_3}{12GJ}\left(\phi_z^c\right)^2 \right). \tag{63}$$

Warping coefficient p_2 already appeared in the parallelogram mechanism analysis of Section 5.1; coefficient p_3 is new and is given by

$$p_3 = 1 + \frac{12 - 6\lambda}{\lambda^2} + \frac{12}{\lambda - \lambda\exp(\lambda)}. \tag{64}$$

Similar to the error motions and actuation load for the sheet flexure and parallelogram mechanism, we have obtained the well-known linear terms, a load-stiffening term in $\bar{M}_z$ due to applied load $\bar{F}_x$, elastokinematic terms linear in the applied loads and quadratic in ϕ_z^c, and a kinematic term in u_x^c that is quadratic in ϕ_z^c. This term describes what is referred to as pivot shift in literature: the deviation of the location of the effective rotation axis of the mechanism [5,15]. Although pivot shift in the x-direction is dominant for $\phi_z^c = 0.15$, it does occur in the y-direction as well, as an effect proportional to the cube of ϕ_z^c [40]. The term does not appear in this analysis because we chose to exclude all third-order terms in a single variable when constructing the series approximation due to the mathematical complexity (even with analytical solver software).

A verification with SPACAR, similar to the one for the parallelogram mechanism, shows that the deviation in the derivatives of the model equations of Eqs. (58)–(63) with respect to the applied loads and the DOF is at most 1.8% for the sheet flexure dimensions and material according to Table 2 and $\phi_z^c = 0.15$. Similar observations for the influence of the warping constraints hold.

6. Conclusion

An accurate approximate closed-form model has been obtained for the spatially deforming sheet flexure subject to a general end-load that includes bending, shear, elongation, torsion and warping deformation. The Hellinger–Reissner variational principle and a suitable set of interpolation functions, tailored to the geometrically nonlinear constraint behavior of a sheet flexure, proved to give a convenient derivation of this model. The resulting model expressions are presented in a format suited for flexure mechanism analysis, in terms of degrees of freedom, error motions, applied loads, and actuation loads. The model captures the nonlinear geometrical stiffness as second-order kinematic and load-stiffening effects, and as third-order elastokinematic effects. The sheet flexure model is verified numerically against FEM. Based on the provided energy scalar for a single sheet flexure, an approach is presented for obtaining closed-form nonlinear models for arbitrary assemblies of sheet flexures connected in parallel. The validity of this approach is illustrated with the cases of the spatial deformation of a parallelogram flexure mechanism and a cross-hinge mechanism.

Declaration of competing interest

The authors declare that they have no known competing financial interests or personal relationships that could have appeared to influence the work reported in this paper.

Acknowledgments

This research was funded by the Innovative Research Incentives Scheme VIDI (Stichting voor de Technische Wetenschappen) (14152 NWO TTW) of the Ministry of Education, Culture and Science of the Netherlands.

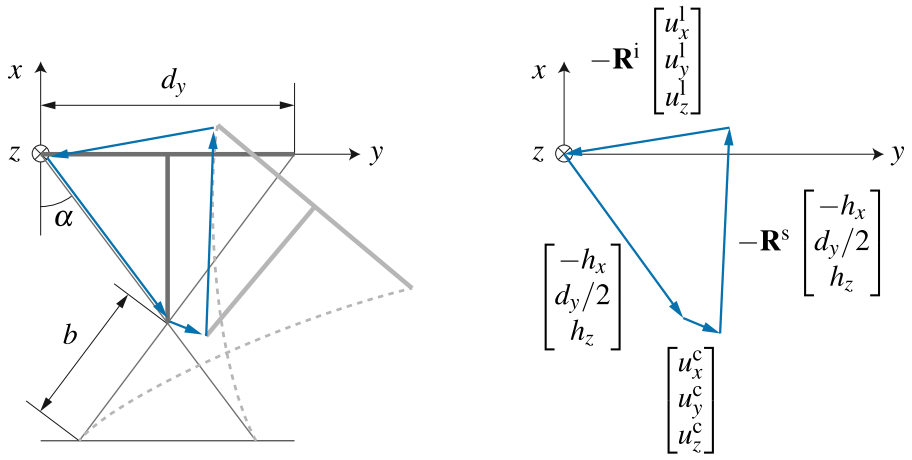

Fig. A.1. Kinematic constraints due to the shuttle of the cross-hinge mechanism.

Appendix. Appendix of article

A.1. Hellinger–Reissner functional for nonuniform torsion

In a potential energy formulation for a fixed–free beam, the total potential energy due to nonuniform torsion is given by

$$\int_0^L \left(\frac{1}{2}GJ\phi_x'^2 + \frac{1}{2}EI_w\phi_x''^2\right)\mathrm{d}s - \bar{M}_x\phi_x(L) - \bar{B}\phi_x'(L), \tag{A.1}$$

where $\bar{M}_x$ represents the torsion moment and $\bar{B}$ the bimoment applied at the free end [21]. Due to the end being fixed, both the rotation and the cross-sectional warping vanish at $s = 0$: $\phi_x(0) = 0$ and $\phi_x'(0) = 0$. Taking variations with respect to the angle of twist $\phi_x(s)$ yields the stationarity conditions

$$GJ\phi_x'' - EI_w\phi_x^{(4)} = 0, \tag{A.2}$$

$$GJ\phi_x'(L) - EI_w\phi_x'''(L) = \bar{M}_x, \tag{A.3}$$

$$EI_w\phi_x''(L) = \bar{B}, \tag{A.4}$$

which represent the equilibrium equations for the beam with constant torsional rigidity GJ and constant warping rigidity EI_w. Boundary condition (A.3) shows that the torsion moment $\bar{M}_x$ is composed of the uniform torsion part $GJ\phi_x'$, which produces shear stress only, and the warping part $-EI_w\phi_x'''$, which plays a role when the cross-sections are not free to warp at the ends, the cross-sectional geometry changes over the beam length, or a torque is applied within the domain $0 < s < L$. In those cases, the warping varies along the beam during torsion and is accompanied by axial strain and hence normal stress and additional shear stress. The finite deformation of a sheet flexure, in which internal loads depend on the deformed configuration, belongs to the last case.

For the derivation of a Hellinger–Reissner-based energy formulation that also explicitly considers the distribution of the internal torsion moment and bimoment along the beam, the total potential energy formulation (in which only variations with respect to ϕ_x are considered) serves as the starting point. The compatibility equations

$$\kappa_x = \phi_x', \tag{A.5}$$

$$\kappa_w = \phi_x'' \tag{A.6}$$

are included in Eq. (A.1) by means of Lagrange multipliers λ_t and λ_w to yield

$$\int_0^L \left(\frac{1}{2}GJ\kappa_x^2 + \frac{1}{2}EI_w\kappa_w^2 + \lambda_t(\phi_x' - \kappa_x) + \lambda_w(\phi_x'' - \kappa_w)\right)\mathrm{d}s - \bar{M}_x\phi_x(L) - \bar{B}\phi_x'(L). \tag{A.7}$$

Variations with respect to κ_x and κ_w then show that $\lambda_t = GJ\kappa_x$ and $\lambda_w = EI_w\kappa_w$, lending λ_t the interpretation of the uniform torsion moment M_{xt} and λ_w the bimoment B. By elimination of κ_x and κ_w, Eq. (A.7) becomes

$$\int_0^L \left(-\frac{M_{xt}^2}{2GJ} + M_{xt}\phi_x' - \frac{B^2}{2EI_w} + B\phi_x''\right)\mathrm{d}s - \bar{M}_x\phi_x(L) - \bar{B}\phi_x'(L), \tag{A.8}$$

representing a Hellinger–Reissner-type energy functional for the independent fields M_{xt}, B and ϕ_x. It is more convenient to have a formulation in terms of the torsion moment instead of M_{xt}. To this end, Eqs. (A.2)–(A.4) can be used to replace M_{xt} by $M_{\bar{x}} + B'$, yielding

$$\int_0^L \left[-\frac{\left(M_{\bar{x}} + B'\right)^2}{2GJ} + M_{\bar{x}}\phi_x' - \frac{B^2}{2EI_w}\right]\mathrm{d}s - \bar{M}_x\phi_x(L) - \left(\bar{B} - B\right)\phi_x'(L). \tag{A.9}$$

Sheet flexures generally have warping constraints at $s = 0$ and $s = L$ as a consequence of a clamping construction or monolithic design. The last term of Eq. (A.9) then vanishes. In the case of a folded sheet flexure [38], which is a single-constraint element that can be regarded as a series assembly of two straight sheet flexures of the current work, the warping of the cross-section is not necessarily constrained at the fold line and the last term may need to be considered.

A.2. Bimoment interpolation

The full expression for the bimoment interpolation is given by

$$\begin{aligned} B = {} & 6\tilde{F}_x I_{\mathrm{te}}\tilde{\phi}_x\left(2\xi - 1\right)/\lambda^2 + 2\tilde{M}_y\left[\tilde{u}_y(-6\xi + 3) + L\tilde{\phi}_z(3\xi - 1)\right]/\lambda^2 \\ & + 2\tilde{F}_z L\left[-3\tilde{u}_y(4 + \lambda^2(2\xi^2 - 3\xi + 1)) + L\tilde{\phi}_z(6 + \lambda^2(3\xi^2 - 4\xi + 1))\right]/\lambda^4 \\ & - \cosh(\lambda\xi)\operatorname{csch}(\lambda)\Big[\tilde{M}_x L/\lambda + 12\tilde{F}_x I_{\mathrm{te}}\tilde{\phi}_x/\lambda^3 \\ & \qquad + \tilde{M}_y\left(6L\tilde{\phi}_z + L\lambda^2\tilde{\phi}_z - 12\tilde{u}_y\right)/\lambda^3 \\ & \qquad + \tilde{F}_z\left(4L^2\tilde{\phi}_z - 6L\tilde{u}_y\right)/\lambda^3\Big] \\ & + \cosh(\lambda - \lambda\xi)\operatorname{csch}(\lambda)\Big[\tilde{M}_x L/\lambda + 12\tilde{F}_x I_{\mathrm{te}}\tilde{\phi}_x/\lambda^3 \\ & \qquad + \tilde{M}_y\left(6L\tilde{\phi}_z - 12\tilde{u}_y\right)/\lambda^3 \\ & \qquad + \tilde{F}_z\left(-8L^2\tilde{\phi}_z + 18L\tilde{u}_y\right. \\ & \qquad \left. + L\lambda^2\tilde{u}_y\right)/\lambda^3\Big], \end{aligned} \tag{A.10}$$

where $\cosh(\xi)$ denotes the hyperbolic cosine function, $\operatorname{csch}(\xi)$

$= 1/\sinh(\xi)$ the hyperbolic cosecant function, λ the dimensionless parameter

$$L\sqrt{GJ/(EI_w)}, \tag{A.11}$$

and ξ the dimensionless coordinate s/L.

A.3. Energy expression

After substitution of the interpolation functions, the full expression for the potential energy of the sheet flexure is given by [27]

$$\begin{aligned}
P = {} & \left(\tilde{M}_x - \tilde{M}_x^{\mathrm{TB}}\right)\tilde{\phi}_x + \left(\tilde{M}_y - \tilde{M}_y^{\mathrm{TB}}\right)\tilde{\phi}_y + \left(\tilde{M}_z - \tilde{M}_z^{\mathrm{TB}}\right)\tilde{\phi}_z \\
& + \left(\tilde{F}_x - \bar{F}_x\right)\tilde{u}_x + \left(\tilde{F}_y - \bar{F}_y\right)\tilde{u}_y + \left(\tilde{F}_z - \bar{F}_z\right)\tilde{u}_z \\
& - \frac{\tilde{F}_x^2 L}{2EA} - \frac{\tilde{F}_z^2 L}{2kGA} - \frac{w_6\tilde{M}_x^2 L}{2GJ} - \frac{\tilde{F}_y^2 L^3}{6EI_z} - \frac{\tilde{F}_y\tilde{M}_z L^2}{2EI_z} - \frac{\tilde{M}_z^2 L}{2EI_z} \\
& - \frac{\tilde{M}_y^2 L}{2EI_y} + \frac{\tilde{M}_y\tilde{F}_z L^2}{2EI_y} - \frac{\tilde{F}_z^2 L^3}{6EI_y} \\
& + \tilde{F}_x L\left(\frac{3}{5L^2}\left[-I_{\mathrm{te}}\tilde{\phi}_x{}^2 - \tilde{u}_y^2\right] + \frac{\tilde{u}_y\tilde{\phi}_z}{10L} - \frac{\tilde{\phi}_z{}^2}{15}\right) \\
& + \tilde{F}_z L\left(\frac{\tilde{\phi}_x\tilde{\phi}_z}{5} - \frac{\tilde{\phi}_x\tilde{u}_y}{10L}\right) + \tilde{M}_y\left(\frac{6\tilde{\phi}_x\tilde{u}_y}{5L} - \frac{\tilde{\phi}_x\tilde{\phi}_z}{10}\right) \\
& + \frac{\tilde{M}_z L}{EI_z}\left(\frac{1}{2}\tilde{F}_x\tilde{u}_y + \frac{1}{12}\tilde{F}_x\tilde{\phi}_z L - \frac{3}{20}\tilde{F}_z\tilde{\phi}_x L + \frac{1}{2}\tilde{M}_y\tilde{\phi}_x\right) \\
& + \frac{\tilde{F}_y L^2}{EI_z}\left(\frac{7}{20}\tilde{F}_x\tilde{u}_y + \frac{1}{30}\tilde{F}_x\tilde{\phi}_z L - \frac{1}{15}\tilde{F}_z\tilde{\phi}_x L + \frac{3}{20}\tilde{M}_y\tilde{\phi}_x\right) \\
& + \frac{\tilde{M}_x L}{GJ}\left(\left[w_4 - 1\right]\tilde{F}_z\tilde{u}_y - \frac{w_5}{6}\tilde{F}_z\tilde{\phi}_z L - w_5\tilde{M}_y\tilde{u}_y/L\right. \\
& \qquad \left. + \left[w_4 - 1\right]\tilde{M}_y\tilde{\phi}_z + w_5\tilde{F}_x I_{\mathrm{te}}\tilde{\phi}_x/L\right) \\
& + \frac{\tilde{F}_x^2 L^3}{EI_z}\left(-\frac{13}{70L^2}\tilde{u}_y^2 - \frac{13}{420L}\tilde{u}_y\tilde{\phi}_z - \frac{1}{210}\tilde{\phi}_z{}^2\right) - \tilde{F}_x^2\frac{I_{\mathrm{te}}^2}{GJL}\left(\frac{3}{5}\tilde{\phi}_x{}^2 w_3\right) \\
& + \frac{\tilde{F}_x\tilde{F}_z L^3}{EI_z}\left(\frac{9}{140L}\tilde{\phi}_x\tilde{u}_y + \frac{1}{60}\tilde{\phi}_x\tilde{\phi}_z\right) \\
& + \tilde{F}_x\tilde{F}_z\frac{I_{\mathrm{te}}}{GJ}\left(\frac{1}{5}L\tilde{\phi}_x\tilde{\phi}_z w_3 - \frac{1}{10}\tilde{\phi}_x\tilde{u}_y w_2\right) \\
& + \frac{\tilde{F}_x\tilde{M}_y L^2}{EI_z}\left(-\frac{9}{70L}\tilde{\phi}_x\tilde{u}_y - \frac{11}{210}\tilde{\phi}_x\tilde{\phi}_z\right) \\
& + \tilde{F}_x\tilde{M}_y\frac{I_{\mathrm{te}}}{GJ}\left(-\frac{1}{10}\tilde{\phi}_x\tilde{\phi}_z w_2 + \frac{6}{5}\tilde{\phi}_x\tilde{u}_y w_3/L\right) \\
& + \frac{\tilde{F}_z^2 L^3}{EI_z}\left(-\frac{19}{1260}\tilde{\phi}_x{}^2\right) + \frac{\tilde{F}_z\tilde{M}_y L^2}{EI_z}\left(\frac{3}{35}\tilde{\phi}_x{}^2\right) + \frac{\tilde{M}_y^2 L}{EI_z}\left(-\frac{13}{70}\tilde{\phi}_x{}^2\right) \\
& + \frac{\tilde{F}_z^2 L^3}{GJ}\left(-\frac{3w_{11}}{70L^2}\tilde{u}_y^2 + \frac{w_{10}}{105L}\tilde{u}_y\tilde{\phi}_z - \frac{2w_9}{105}\tilde{\phi}_z{}^2\right) \\
& + \frac{\tilde{F}_z\tilde{M}_y L^2}{GJ}\left(\frac{w_2}{10L^2}\tilde{u}_y^2 - \frac{w_8}{5L}\tilde{u}_y\tilde{\phi}_z + \frac{w_7}{30}\tilde{\phi}_z{}^2\right) \\
& + \frac{\tilde{M}_y^2 L}{GJ}\left(-\frac{3w_3}{5L^2}\tilde{u}_y^2 + \frac{w_2}{10L}\tilde{u}_y\tilde{\phi}_z - \frac{w_1}{15}\tilde{\phi}_z{}^2\right).
\end{aligned} \tag{A.12}$$

The coefficients w_i are solely functions of λ and given by Eq. (A.13).

$$\begin{aligned}
w_1 &= \frac{180\left(\lambda^2+6\right)\mathrm{csch}(\lambda) + 2\lambda\left(\lambda^4+30\lambda^2+270\right) - 15\left(\lambda^4+12\lambda^2+72\right)\coth(\lambda)}{2\lambda^5}, \\
w_2 &= \frac{\lambda\left(\lambda^4+720\right) - 120\left(\lambda^2+12\right)\tanh\left(\frac{\lambda}{2}\right)}{\lambda^5}, \\
w_3 &= \frac{\lambda^5 - 10\lambda^3 + 120\lambda - 240\tanh\left(\frac{\lambda}{2}\right)}{\lambda^5}, \\
w_4 &= \frac{\lambda\left(\lambda^2-6\right) + \left(\lambda^2+12\right)\tanh\left(\frac{\lambda}{2}\right)}{\lambda^3}, \\
w_5 &= \frac{\lambda^3 - 12\lambda + 24\tanh\left(\frac{\lambda}{2}\right)}{\lambda^3}, \\
w_6 &= \frac{\exp(\lambda)(\lambda-2) + \lambda + 2}{(\exp(\lambda)+1)\lambda}, \\
w_7 &= \frac{120\left(\lambda^2-6\right)\coth(\lambda) + 240\left(\lambda^2+3\right)\mathrm{csch}(\lambda) + \left(\lambda^2-30\right)\lambda^3}{\lambda^5}, \\
w_8 &= \frac{\lambda^5 - 10\lambda^3 + 5\left(\lambda^4+24\lambda^2+120\right)\mathrm{csch}(\lambda) + 180\lambda - 600\coth(\lambda)}{\lambda^5}, \\
w_9 &= \frac{\lambda^6 - 14\lambda^4 + 420\lambda^2 - 420\lambda(5\cosh(\lambda)+4)\mathrm{csch}(\lambda) + 3780}{\lambda^6}, \\
w_{10} &= \frac{\lambda^6 + 63\lambda^4 + 5040\lambda^2 - 420\lambda\left(\lambda^2 + 2\left(\lambda^2+21\right)\cosh(\lambda) + 30\right)\mathrm{csch}(\lambda) + 30240}{\lambda^6}, \\
w_{11} &= -\frac{420\lambda\left(\lambda^2+18\right)\mathrm{csch}(\lambda) + 35\lambda\left(\lambda^4+36\lambda^2+360\right)\coth(\lambda) - 3\left(\lambda^6+84\lambda^4+1540\lambda^2+6720\right)}{3\lambda^6}.
\end{aligned} \tag{A.13}$$

The definition of these coefficients is such that their limit is 1 when $\lambda \to \infty$.

A.4. Warping coefficients sheet flexure model

The model expressions for the sheet flexure contain the coefficients c_i that account for the warping deformation. Their definition in terms of the w_i from Eq. (A.13) is given by

c_1	$1/w_6$	c_{11}	$6w_3/5 - w_5^2/w_6$
c_2	$-6/5 + 2w_5/w_6$	c_{12}	$2w_1/15 - (w_4-1)^2/w_6$
c_3	$-w_5/w_6$	c_{13}	$-w_2/10 + (w_4-1)w_5/w_6$
c_4	$(w_4-1)/w_6$	c_{14}	$6w_3/5 - w_5^2/w_6$
c_5	$(w_4-1)/w_6$	c_{15}	$-w_5^2/(36w_6) + 4w_9/105$
c_6	$-w_5/(6w_6)$	c_{16}	$(w_4-1)w_5/(6w_6) - w_{10}/105$
c_7	$3/5 - w_5/w_6$	c_{17}	$-(w_4-1)^2/w_6 + 3w_{11}/35$
c_8	w_5/w_6	c_{18}	$-w_3/5 + w_5^2/(6w_6)$
c_9	$(w_4-1)/w_6$	c_{19}	$(w_4-1)w_5/(6w_6) - w_7/30$
c_{10}	$w_5/(6w_6)$	c_{20}	$\left[-30(w_4-1)^2 - 5w_5^2 + 6w_6w_8\right]/(60w_6)$

(A.14)

The full model equations are available for download [27].

A.5. Derivation of kinematic constraints due to the shuttle

Fig. A.1 shows the vectors used in Eq. (43) for the kinematic relation that the shuttle enforces between the two sheet flexure ends of the cross-hinge flexure mechanism. Parameter d_y is the shuttle length. Parameters h_x and h_z represent the distance between the sheet flexure ends and the center of compliance, as measured along the x-axis and z-axis, respectively.

A.6. Warping coefficients parallelogram mechanism

The full expressions for the warping coefficients of the parallelogram mechanism of Section 5.1 are given by

$$p_1 = 1 + \frac{16128}{\lambda^6} + \frac{2688}{\lambda^4} + \frac{588}{5\lambda^2} - \coth(\lambda/2)\left(\frac{8064}{\lambda^5} + \frac{672}{\lambda^3} + \frac{14}{\lambda}\right), \tag{A.15}$$

$$p_2 = \frac{120 + 60\lambda + 12\lambda^2 + \lambda^3 + \exp(\lambda)\left(-120 + 60\lambda - 12\lambda^2 + \lambda^3\right)}{2\lambda^2 + \lambda^3 + \lambda^2\exp(\lambda)(-2+\lambda)}. \tag{A.16}$$

References

[1] Eastman FS. Flexure pivots to replace knife edges and ball bearings. In: Engineering Experiment Station Bulletin 86. Seattle, WA: University of Washington; 1935.

[2] Jones RV. A parallel-spring cross-movement for an optical bench. J Sci Instrum 1956;33(7):279–80.

[3] Smith ST. Flexures: Elements of Elastic Mechanisms. Boca Raton, FL: CRC Press; 2000.

[4] Slocum AH. Precision Machine Design. Englewood Cliffs, NJ: Prentice Hall; 1992.

[5] Haringx JA. The cross-spring pivot as a constructional element. Appl Sci Res 1949;1(1):313–32.

[6] Awtar S. Analysis and Synthesis of Parallel Kinematic XY Flexure Mechanisms (Ph.D. thesis), Cambridge, MA: Massachusetts Institute of Technology; 2003.

[7] Sen S. Beam Constraint Model: Generalized Nonlinear Closed-form Modeling of Beam Flexures for Flexure Mechanism Design (Ph.D. thesis), Ann Arbor: University of Michigan; 2013.

[8] Awtar S, Slocum AH, Sevincer E. Characteristics of beam-based flexure modules. J Mech Des 2007;129(6):625–39.

[9] Awtar S, Sen S. A generalized constraint model for two-dimensional beam flexures: nonlinear load-displacement formulation. J Mech Des 2010;132(8):081008:1–11.

[10] Sen S, Awtar S. A closed-form nonlinear model for the constraint characteristics of symmetric spatial beams. J Mech Des 2013;135(3):031003:1–11.

[11] Bai R, Awtar S, Chen G. A closed-form model for nonlinear spatial deflections of rectangular beams in intermediate range. Int J Mech Sci 2019;160:229–40.

[12] Nijenhuis M, Meijaard JP, Mariappan D, Herder JL, Brouwer DM, Awtar S. An analytical formulation for the lateral support stiffness of a spatial flexure strip. J Mech Des 2017;139(5):051401:1–11.

[13] Nijenhuis M, Brouwer DM. A closed-form model for the support stiffness of spatial flexure strips with limited twist. In: ASME 2016 International Design Engineering Technical Conferences and Computers and Information in Engineering Conference. Charlotte, NC, USA: ASME; 2016, p. 1–10, V05AT07A027.

[14] Brouwer DM, Meijaard JP, Jonker JB. Large deflection stiffness analysis of parallel prismatic leaf-spring flexures. Precis Eng 2013;37(3):505–21.

[15] van Eijk J. On the Design of Plate-Spring Mechanisms (Ph.D. thesis), Delft: Delft University of Technology; 1985.

[16] Timoshenko S, Goodier JN. Theory of Elasticity. New York, NY: McGraw-Hill; 1969.

[17] Love AEH. A Treatise on the Mathematical Theory of Elasticity. Fourth edition. Cambridge: Cambridge University Press; 1927.

[18] Lang H, Linn J, Arnold M. Multi-body dynamics simulation of geometrically exact Cosserat rods. Multibody Syst Dyn 2011;25(3):285–312.

[19] Reissner E. On one-dimensional large-displacement finite-strain beam theory. Stud Appl Math 1973;52:87–95.

[20] Cullimore MSG. The shortening effect - a non-linear feature of pure torsion. Eng Struct 1949;153–64.

[21] Timoshenko S, Gere JM. Theory of Elastic Stability. second ed.. New York, NY: McGraw-Hill; 1961.

[22] Cowper GR. The shear coefficient in Timoshenko's beam theory. J Appl Mech 1966;33(2):335–40.

[23] Timoshenko S. On the torsion of a prism, one of the cross-sections of which remains plane. In: Proceedings of the London Mathematical Society. 2nd Series, vol. 20, 1922, p. 389–97.

[24] Lanczos C. The Variational Principles of Mechanics. Mathematical Expositions, No. 4, Toronto: University of Toronto Press; 1949.

[25] Awtar S, Sen S. A generalized constraint model for two-dimensional beam flexures: nonlinear strain energy formulation. J Mech Des 2010;132(8):081009:1–11.

[26] Washizu K. Variational Methods in Elasticity and Plasticity. Third ed.. Oxford, New York: Pergamon Press; 1982.

[27] Nijenhuis M. Third-order spatial sheet flexure model. 2020, Accessed on July 1, 2020. URL http://marijnnijenhuis.nl/sheet.

[28] Plainevaux JE. Etude des déformations d'une lame de suspension élastique. Il Nuovo Cimento 1956;4(4):922–8.

[29] Nijenhuis M, klein Avink STB, Dierkes WK, Noordermeer JWM, Brouwer DM. Improved dynamic performance in flexure mechanisms by overconstraining using viscoelastic material. Precis Eng 2020;63:115–25.

[30] Jonker JB, Meijaard JP. SPACAR — Computer program for dynamic analysis of flexible spatial mechanisms and manipulators. In: Schiehlen W, editor. Multibody Systems Handbook. Berlin: Springer; 1990, p. 123–143.

[31] Jonker JB, Meijaard JP. A geometrically non-linear formulation of a three-dimensional beam element for solving large deflection multibody system problems. Int J Non-Linear Mech 2013;53:63–74.

[32] Jonker JB. Implementation of shear deformable thin-walled beam element for flexible multibody dynamics. In: Proceedings of the 8th ECCOMAS Thematic Conference on Multibody Dynamics 2017. Prague, Czech Republic; 2017, p. 141–162.

[33] Trahair NS. Nonlinear elastic nonuniform torsion. J Struct Eng 2005;131(7):1135–42.

[34] Meijaard JP. The importance of imperfections in leaf-spring flexures for the support stiffness. Procedia IUTAM 2015;13:82–9.

[35] Nijenhuis M. Spatial flexure mechanism analysis (Ph.D. thesis), Enschede: University of Twente; 2020.

[36] Ashwell DG. The anticlastic curvature of rectangular beams and plates. Aeronaut J 1950;54(479):708–15.

[37] Meijaard JP. Refinements of classical beam theory for beams with a large aspect ratio of their cross-sections. In: IUTAM Symposium on Dynamics Modeling and Interaction Control in Virtual and Real Environments. Budapest, Hungary; 2011, p. 285–292.

[38] Soemers HMJR. Design Principles: For Precision Mechanisms. Enschede: T-pointpress; 2011.

[39] Plainevaux JE. Mouvement de tangage d'une suspension élémentaire sur lames élastiques. Il Nuovo Cimento 1956;4(5):1133–41.

[40] Hongzhe Z, Shusheng B. Accuracy characteristics of the generalized cross-spring pivot. Mech Mach Theory 2010;45(10):1434–48.